THE PENNSYLVANIA STATE UNIVERSITY
SCHREYER HONORS COLLEGE

DEPARTMENT OF MATERIALS SCIENCE AND ENGINEERING

Synthesis of KNN Thin Films Through Pulsed Laser Deposition
for Piezoelectric Micromachined Ultrasonic Transducers

KALEB JESSE STERLING
SPRING 2021

A thesis
submitted in partial fulfillment
of the requirements
for a baccalaureate degree
in Materials Science and Engineering
with honors in Materials Science and Engineering

Reviewed and approved* by the following:

Susan Trolier-McKinstry
Evan Pugh University Professor and Steward S. Flaschen
Professor of Ceramic Science and Engineering
Thesis Supervisor

Robert Allen Kimel
Assistant Professor of Materials Science and Engineering
Honors Adviser

* Electronic approvals are on file.

ABSTRACT

This thesis explores optimization of a pulsed laser deposition process to synthesize high-quality potassium sodium niobate (KNN) thin films for use in piezoelectric micromachined ultrasonic transducers (pMUTs). The chemical and thermal interactions during calcination were investigated as well as sintering of a bulk KNN target from powder precursors. The implementation of two calcination processes at 750°C and a sintering process at 1075°C produced bulk KNN targets of high density

KNN thin films were deposited onto platinized silicon substrates through pulsed laser deposition. The microstructure and phase purity were evaluated in the resultant films. Significant parameter variation was enacted onto the pulsed laser deposition process, based on parameter effects documented in literature and observation, to produce thin film characteristics that predict high piezoelectric performance. The platinized silicon substrate was aligned to the KNN target at varied target-to-substrate distance of 5.7 cm. The deposition ambient reached a base pressure of $2.2 \cdot 10^{-7}$ Torr before being increased to a deposition ambient pressure of 400 mTorr. The substrate temperature was set to 550°C and the pulse rate of the excimer laser was set to 5 Hz for a deposition duration of 6 minutes. The substrate was allowed to cool to room temperature at a cooling ambient pressure of 400 mTorr. The resultant pulsed laser deposition parameters yielded KNN thin films with high phase purity, but exhibited suboptimal microstructures featuring high surface roughness and porosity.

Post-deposition thermal annealing processes were subsequently added to improve the thin film microstructure while retaining phase purity. Initial investigation into annealing optimization yielded phase pure polycrystalline thin films with improved microstructure at 700°C for 5 minutes, suggesting that further optimization of the annealing process, along with investigation into KNN doping, could produce high quality KNN thin films suitable for implementation into pMUTs.

The electrical characteristics of the resultant film were as follows: the remanent polarization (P_r) was 10.7 $\mu C/cm^2$, the maximum polarization (P) was 12.7 $\mu C/cm^2$, the dielectric constant (ε_r) was 605. The loss tangent ($tan\delta$) was 2.8%.

TABLE OF CONTENTS

LIST OF FIGURES

LIST OF TABLES

ACKNOWLEDGEMENTS

Firstly, I would like to thank my research partner, Donovan Moses, for his dedication and support throughout this study. Though the purpose of our studies were different, we conducted the synthesis optimization conjointly and I would not have been able to achieve nearly as much without his partnership. I would also like to thank all the members of the STM group and the staff of the Materials Research Institute for serving as incredible resources during my time spent learning and growing here at Penn State. I would like to thank Nathan Bishop, Beth Jones, and Wanlin Zhu specifically for their immense contributions to supporting this study and providing much needed assistance and insight. They went well beyond the line of duty to assure that our investigation went as smoothly as possible.

Lastly, I would like to offer my sincerest gratitude to my thesis supervisor Dr. Susan Trolier-McKinstry for her outstanding mentorship and support. I aspire to one day reflect the same knowledge and passion for materials science that she exudes effortlessly. I could not thank her enough for developing me into the materials scientist that I am today.

Chapter 1: Introduction

1.1 Research Scope and Purpose

Lead-based thin films, namely those made of $Pb(Zr,Ti)O_3$ (PZT), have been extensively utilized in microelectromechanical systems (MEMS) due to their high dielectric and piezoelectric properties. $(K_{0.50}Na_{0.50})NbO_3$ (KNN), a composition of the solid solution $KNbO_3$ (KN) and $NaNbO_3$ (NN), exhibits lower piezoelectric performance relative to PZT; however, its lead-free composition and lack of toxicity makes it an environmentally friendly alternative to PZT. The use of high-quality KNN thin films in the large-scale manufacture and implementation of piezoelectric MEMS devices will likely occur in the near future. This project explores the synthesis of KNN thin films through pulsed laser deposition, specifically for use in piezoelectric micromachined ultrasonic transducers (pMUTs), and compares achieved film structure and piezoelectric performance to state-of-the-art, RF magnetron sputtered, KNN thin films, in order to quantify the viability of this deposition method for the synthesis of this promising alternative.

1.2 Considerations in Engineering and Design

1.2.1 Economic

The pulsed laser deposition process is relatively cost effective when compared to other physical vapor deposition techniques. Since the emitted plasma plume from laser ablation is confined and highly directional, the substrate area is limited to a few square centimeters, at maximum. While this generally prohibits the use of pulsed laser deposition in large-scale industrial manufacturing, it is beneficial in research applications as process optimization can be conducted without significant waste. In this study,

the F_2 gas required to run the KrF excimer laser was costly. Therefore, refilling the F_2 gas was postponed until the laser needed to be recharged to operate, maximizing canister use.

1.2.2 Environmental

Investigating KNN's ability to serve as an environmentally friendly alternative to PZT was of interest in this study. KNN is synthesized from potassium carbonate (K_2CO_3), sodium carbonate (Na_2CO_3), and niobium(V) oxide (Nb_2O_5) powder precursors. None of the precursors or their intermediates pose environmental threats due to toxicity, a strong argument for the long-term implementation of KNN. However, extracting niobium(V) oxide and other powder precursors through mining generates harmful waste. In this study, the use and disposal of these materials was highly regulated; nevertheless, the environmental impact of precursor mining should be considered if KNN proves to be a viable alternative to PZT.

1.2.3 Sustainability

There is no question that this project services a sustainable need. The market for MEMs devices is large and predicted to expand in the near-future due to the onset of the Internet of Things. pMUT devices already serve a large role in biomedical applications including but not limited to: ultrasonic actuation, medical imaging, and particle and cell manipulation. These demands will likely create a well-defined market for KNN thin films.

1.2.4 Manufacturability

The purpose of this study was to investigate the ability of pulsed laser deposition to synthesize high quality KNN thin films. Pulsed laser deposition is a technique that is primarily suitable for research purposes as the technique is highly unscalable. As such, manufacturability was not of considerable concern for this study.

1.2.5 Ethical

All results produced from this study are presented unaltered. Data that was procured during the study, but omitted from discussion in this thesis is purely for the sake of clarity. All rationale and methodology are conveyed concisely.

1.2.6 Health and Safety

The health and safety of the researchers and staff was of upmost priority. Safety protocols, including personal use of PPE and the implementation of engineering controls, were strictly adhered to during all phases of research. Additional COVID-19 specific safety measures were strictly followed to assure reduction of viral spread while maintaining high productivity.

1.2.7 Social and Political

None of the researchers involved in this study took part in any conflict that extended past driving ethical scientific discovery.

Chapter 2: Literature Review

2.1 Electronic Properties of Materials

2.1.1 Ferroelectricity

Ferroelectricity is a material property in which the spontaneous polarization of a material can be reoriented between crystallographically equivalent directions through the application of a realizable electric field. The polarization change is at least partially retained after the electric field has been removed [1]. Typically, ferroelectricity is observed over a specific temperature range for a given material. Most ferroelectric materials reach their maximum dielectric permittivity at the Curie temperature (T_C); dielectric permittivity decreases with increasing temperature above T_C, according to the Curie-Weiss law for second order phase transitions:

$$K = \frac{1}{\varepsilon_r} = \frac{C}{T - T_C} \qquad \textbf{2.1}$$

where K is the dielectric constant, ε_r is the relative permittivity, and C is the material-specific Curie constant [2]. For ferroelectrics undergoing first order transitions, T_C is replaced by θ, the Curie-Weiss temperature. The ferroelectric response can be observed by measuring the dielectric polarization when a large alternating electric field is applied. This produces a polarization-electric field (P-E) hysteresis loop, as seen in **Figure 2.1**.
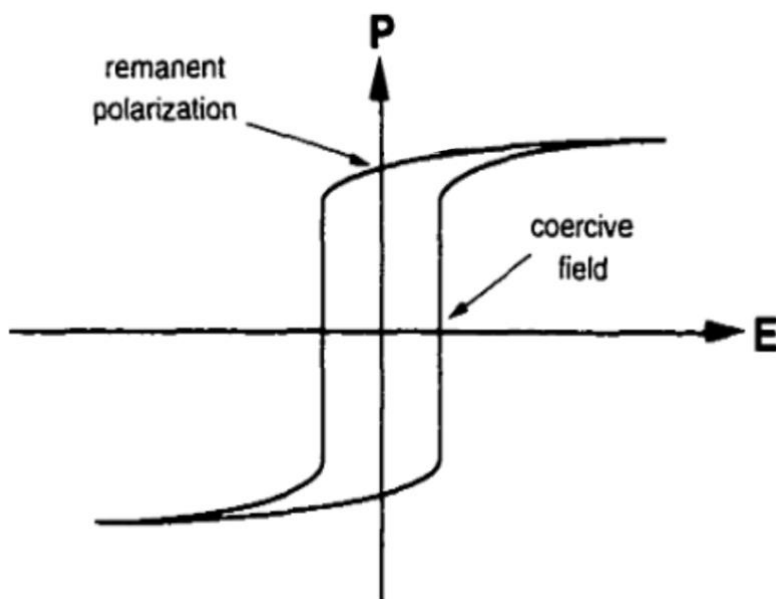
Figure 2.1: Schematic of polarization-hysteresis loop for a ferroelectric material, adapted from [3]

Two significant characteristics of a material's ferroelectric character are obtained from the measured P-E hysteresis loop: the remanent polarization (P_r) and the coercive field (E_C). The remanent polarization is the value of the polarization at zero applied electric field. The coercive field is the applied electric field at which the net polarization is equal to zero (i.e., the electric field strength required to reorient the spontaneous polarization).

The allowed crystallographically defined directions of the polarization vectors in distorted perovskites are shown in **Table 2.1**.

Table 2.1: Polar axes (referred to the cubic prototype) of ferroelectric perovskite crystal structures [4]

Crystal Structure	Polar axes (number of possible orientations)
Tetragonal	<001> (6)
Orthorhombic	<110> (12)
Rhombohedral	<111> (8)

In a ferroelectric material, there are regions within the crystal where the spontaneous polarization vectors are uniformly oriented in a given crystallographic direction [5]. These regions are called domains; they exist in both polycrystalline and single crystal samples. Domains minimize mechanical and electrostatic energy upon cooling the sample through the ferroelectric transition temperature [5]. The domains in a ferroelectric material can be aligned by the application of a large electric field, through an effect known as poling, illustrated in **Figure 2.2**.

before poling, $P_R = 0$ after poling, $P_R \neq 0$
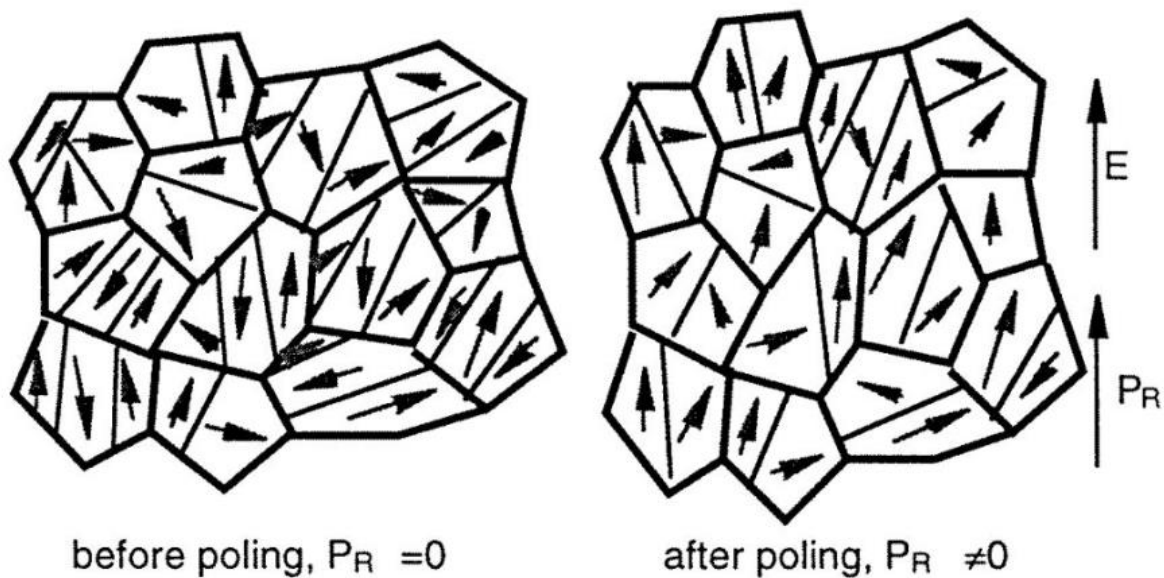
Figure 2.2: Schematic of the poling effect on a polycrystal with randomly oriented domains, adapted from [5]. Dark boundaries are grain boundaries, whereas thinner lines are domain walls. Arrows denote the polarization direction

2.1.2 Piezoelectricity

All ferroelectric materials can exhibit piezoelectricity, in which mechanical stress or strain is linearly coupled with an electric field or polarization. In the direct piezoelectric effect, an induced polarization is generated through the application of a mechanical stress. This is characterized by the equation:

$$D_i = \sum d_{ik}\sigma_k \ \text{ or } D_i = \sum e_{ik}x_k \qquad\qquad \textbf{2.2}$$

where D_i is the electric displacement field ($i = 1\ to\ 3$), σ_i is the strain tensor ($i = 1\ to\ 6$), x_i is the strain tensor ($i = 1\ to\ 6$), and d_{ik} and e_{ik} are the 3rd rank tensor piezoelectric coefficients. In the converse piezoelectric effect, a strain is generated through application of an electric field. This is characterized by the equation:

$$x_i = \sum d_{ki} E_k \text{ or } \sigma_i = - \sum e_{ki} E_k \qquad\qquad \textbf{2.3}$$

where E_k is the applied electric field ($i = 1\ to\ 3$).

Piezoelectricity can only occur within crystal classes that are non-centrosymmetric, as the movement of positive and negative ions will result in an electric dipole [2]. Of the 21 crystal classes that are non-centrosymmetric, 20 of them exhibit piezoelectricity (crystal class 432 contains other symmetry elements that preclude piezoelectricity) [2]. Furthermore, only 10 of the non-centrosymmetric crystal classes contain a unique polar axis and therefore can potentially exhibit ferroelectricity [2].

2.1.2.1 Contributions to the Piezoelectric Response

The net piezoelectric behavior of a ferroelectric material is often due to the sum of intrinsic and extrinsic contributions. Forming these contributions are three dominant mechanisms as illustrated in **Figure 2.3**: polarization extension, polarization rotation, and the motion of domain walls [6].
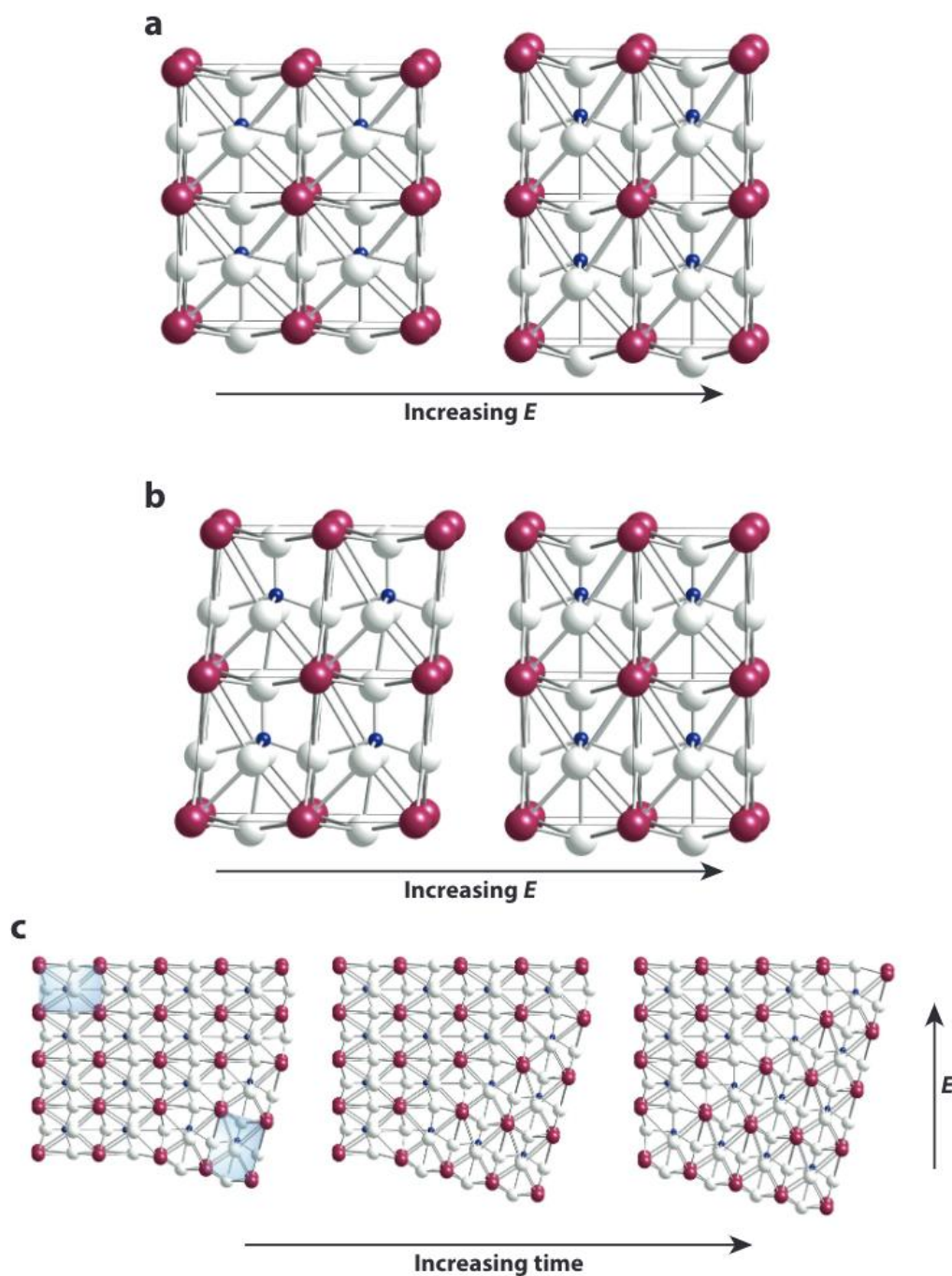
Figure 2.3: Schematics illustrating the three dominant mechanisms producing the piezoelectric response for the ABX$_3$ perovskite structure, adapted from [6]. a) Polarization extension for the case when both the spontaneous polarization and the applied electric field are pointed in the up direction. b) Polarization rotation for an electrical field oriented in the up direction. c) Domain wall motion. Two domains are shown (as seen by the shaded boxes). As an electric field is applied, the domain wall moves, changing the volume fraction of the two domains shown. The A-site is pink, the B-site is blue, the X-site is white.

The intrinsic response is generated from the averaged polarization-induced strain within a domain and is the resultant sum of polarization extension and polarization rotation mechanisms [7][6]. This represents the entire piezoelectric response for single domain single crystals [7].

The extrinsic response is generated from the strain induced from the movement of domain walls or phase boundaries in response to the applied electric field or mechanical stress [7][6]. Non-180º domain walls dominate the extrinsic piezoelectric effect in most samples due to the ferroelastic distortion inducing change in the material strain [5][6], as illustrated in **Figure 2.3**. 180º domain walls have also been proven to contribute to the extrinsic piezoelectric response, albeit at comparatively small magnitudes [8].

2.2 Potassium Sodium Niobate

2.2.1 Structure

Potassium sodium niobate $(K_xNa_{1-x})NbO_3$ (KNN), a solid solution of $KNbO_3$ (KN) and $NaNbO_3$ (NN), is of interest for use in microelectromechanical devices due to its high Curie temperature (~400ºC), reasonable piezoelectric response, and environmentally-friendly constituents. In KNN, the non-centrosymmetric perovskite crystal produces the piezoelectric response. As an ABX_3 perovskite, potassium and sodium ions interchange at the A-site, niobium cations populate the B-site, and oxygen anions (X) occupy the face centers. The B-site is slightly displaced to the oxygen octahedra, resulting in an electric dipole. The spontaneous polarization of the crystal unit results in ferroelectricity.
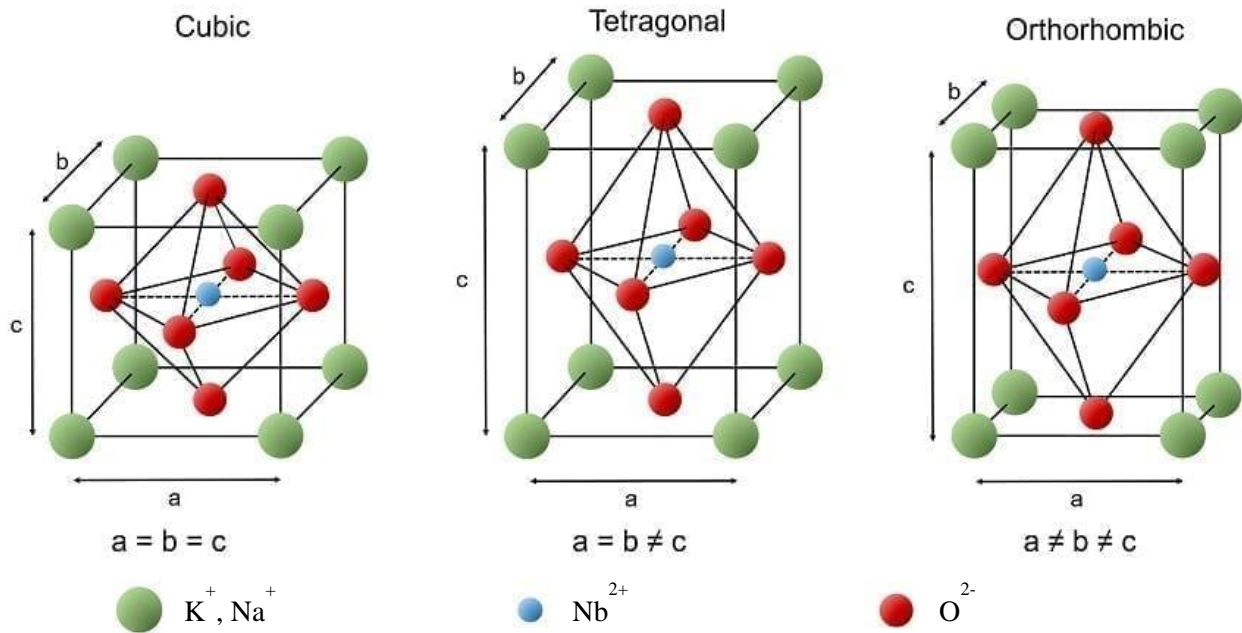
Figure 2.4: Schematic of the cubic, tetragonal, and orthorhombic crystal structures for a ABX₃ perovskite material, shown for KNN, adapted from [9]

2.2.2 Piezoelectric Properties

KNN exhibits lower piezoelectric properties relative to PZT, as shown in **Table 2.2**. However, it does not

contain lead and is therefore sometimes believed to be more environmentally-friendly.

Table 2.2: Piezoelectric properties of PZT and KNN thin films deposited through pulsed laser deposition [10]

	P_r	$d_{33,f}$	$d_{31,f}$	$e_{31,f}$
	[$\mu C/cm^2$]	[pm/V]	[pm/V]	[C/m^2]
PZT	18.4	116	-97	-14.3
KNN	12.6	58	-42	-5.6

When the composition of KNN lies on a morphotropic phase boundary, where a structural change of the

material is independent of temperature and due entirely to compositional instability, its piezoelectric

response is maximized over a wide temperature range. The KNN phase diagram, shown in **Figure 2.5**, contains three separate morphotropic phase boundaries at room temperature. The composition of KNN of focus in this study is $(K_{0.50}Na_{0.50})NbO_3$, which lies on a morphotropic phase boundary between two distinct ferroelectric orthorhombic crystal systems, denoted in **Figure 2.5** by the green region.
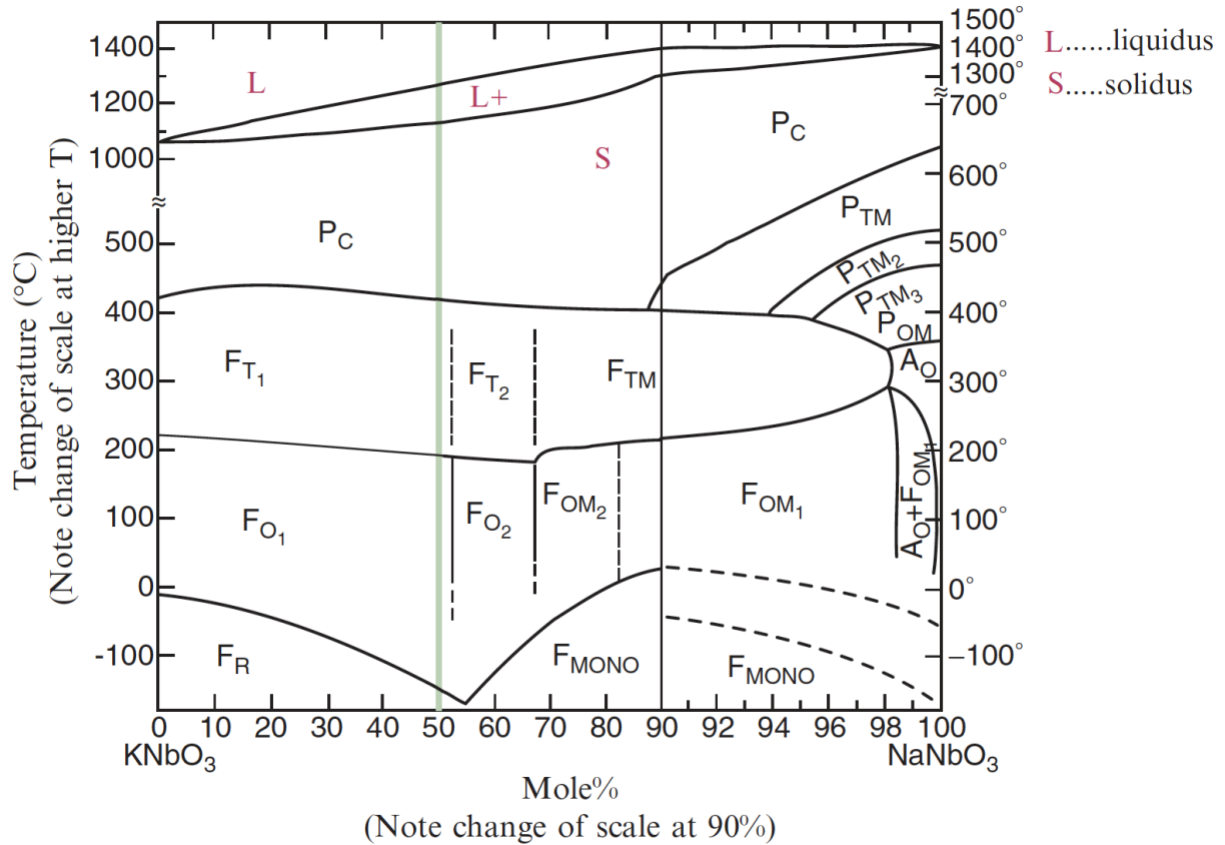
Figure 2.5: Binary phase diagram for the $(K_xNa_{1-x})NbO_3$ solid solution, adapted from [2]. P_C is the paraelectric cubic form, F_T is the ferroelectric tetragonal form, F_O is the ferroelectric orthorhombic form, F_R is the ferroelectric rhombohedral form, and F_{MONO} is the ferroelectric monoclinic form.

2.3 Pulsed Laser Deposition

2.3.1 Development of Pulsed Laser Deposition

Pulsed laser deposition is a form of physical vapor deposition, a process characterized by the initial vaporization of a solid material, transport of the vapor phase through a vacuum, then condensation into a thin film.

In pulsed laser deposition, the bulk material is rapidly ablated with a pulsed laser producing an energetic ion plasma plume, which subsequently condenses onto a heated substrate situated perpendicular to the
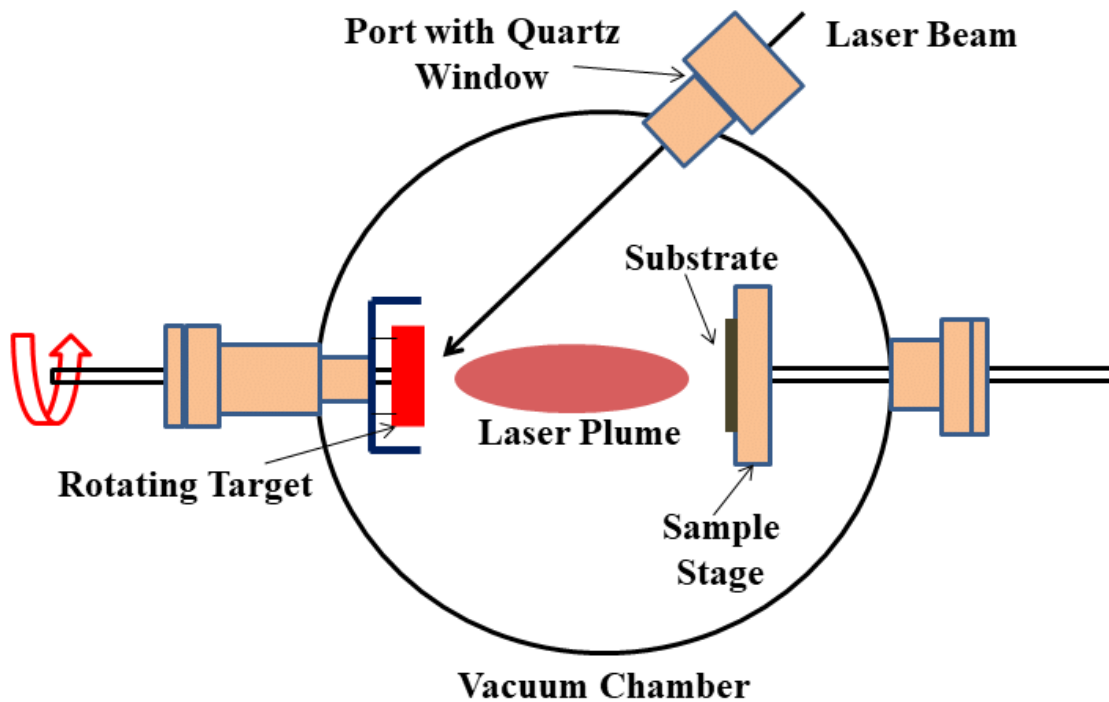
Figure 2.6: Schematic representation of the pulsed laser deposition process, adapted from [11]

target's surface, as illustrated in **Figure**
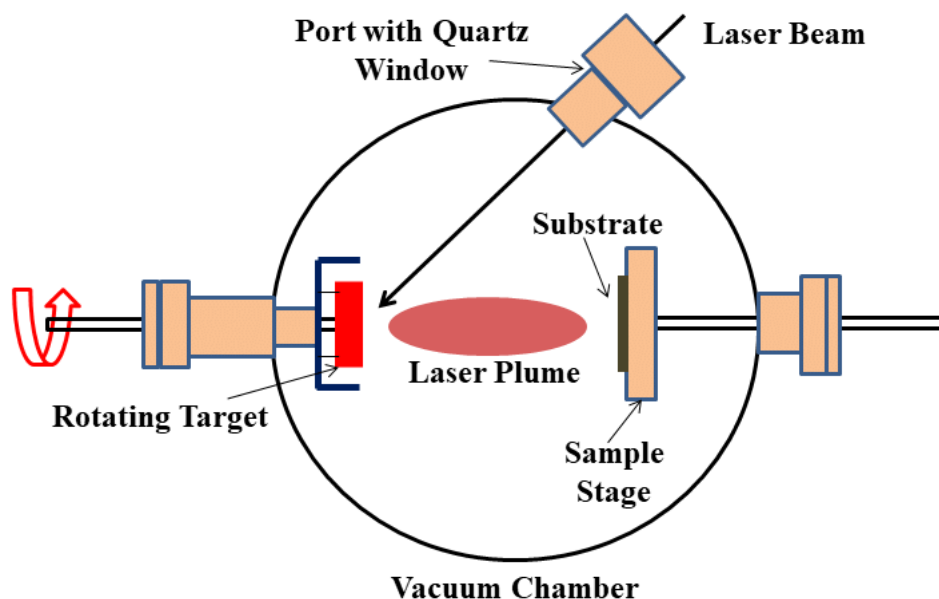
2.6.

The utilization of pulsed laser ablation of a solid source to transfer material to a substrate was first demonstrated in the work of Howard M. Smith and A. F. Turner in 1965 [12]. The study consisted of a Trion ruby laser, operating at a 3 J energy output and a 1/60 Hz frequency, ablating several powdered materials in a 10^{-4} Torr vacuum [12]. Though the obtained films showed significant evidence of non-stoichiometry and macroparticulate ejection, challenges still encountered today, Smith and Turner emphasized the key advantages for the technique: the high film growth rate and the "ultraclean" film formation conditions [12]. In the years following, several developments improved the appeal of this technique. In 1975, the ability to produce stoichiometric intermetallic materials was demonstrated by J. Dessere and J. F. Eloy [13]. In 1983, the first instance of high temperature superconductive oxides deposited through pulsed laser deposition were reported by Zaitsev-Zotov et al [14]. But perhaps the most significant breakthrough for the technique was the 1987 discovery that pulsed laser deposition of superconductive epitaxial $YBa_2Cu_3O_{7-\delta}$ (YBCO) films drastically increased the critical current density and allowed for complex stoichiometric compositions previously difficult to achieve through alternative techniques [15]. These breakthroughs in high Curie

temperature superconducting oxides, among others, paved the way for PLD implementation into perovskite thin film oxides, of interest for their ferroelectric, dielectric, and magnetic properties.

2.3.2 Ablation, Plasma Formation, and Stoichiometry

The process of photon conversion to thermal, mechanical, and chemical energy through laser ablation, was initially of interest for its application in laser machining. The resultant plasma plume was soon recognized

two shaded regions corrspond
to different distributions of
material in the laser plasma

small spots correspond to
macroparticles ejected from surface
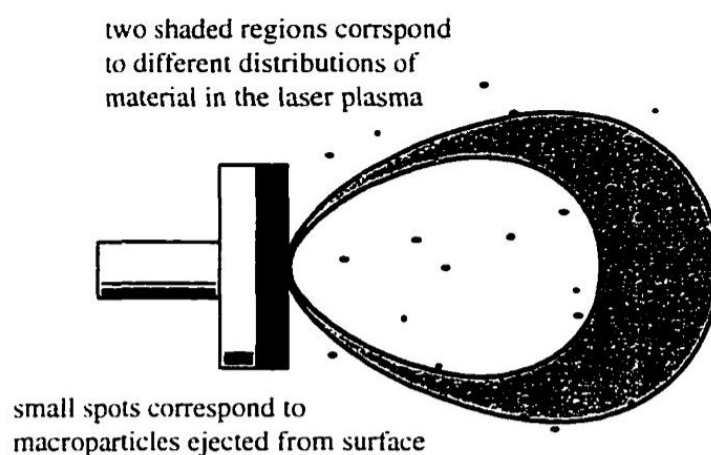
Figure 2.7: Schematic of a laser-induced plasma plume, adapted from [4]

to be a potential vehicle for film growth due to the high energy density of pulsed laser technology allowing for congruent vaporization [16]. A schematic for the typical shape and regions of a plasma plume is depicted in **Figure 2.7**.

The bright region of **Figure 2.7** corresponds to the brilliant plasma plume visible during deposition, and consists of the energetic species that can bombard the surface of the substrate [16].

In 1991, L. Wiedeman and H. Helvajian conducted a study into the laser photodecomposition of sintered YBCO which revealed significant insight into the plasma plume. A schematic representation of some of their important conclusions is depicted in **Figure 2.8**.
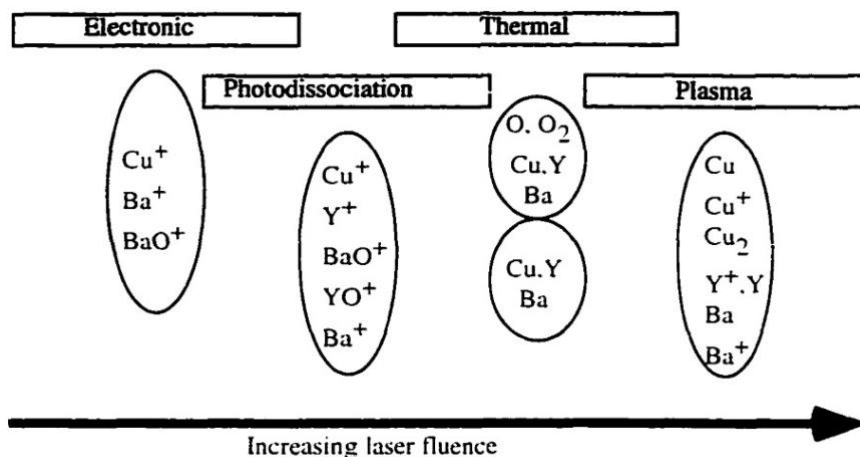
Figure 2.8: Schematic of the effect of laser fluence on material removal mechanisms, adapted from [4]

Wiedeman and Helvajian found that an emitted species could not be detected below a minimum energy level. At low laser fluence, a visible plasma plume was not detected, the majority of emitted species were either atomic or diatomic, and most importantly, the kinetic energies of all emitted species were identical, within experimental error [16]. These results indicate that the predominant excitation mechanism within this region is electronic.

At middling laser fluence, a brilliant plasma plume was clearly visible, the emitted species consisted of mainly anionic material, and a bimodal kinetic energy distribution was observed with higher energy levels for the ionic species. These results indicate that the predominating excitation mechanism in this region is thermal desorption.

At high laser fluence, the bimodal kinetic energy distribution became significantly more pronounced, indicating that high laser energy disproportionately excites ionic particles while rendering the neutral species, emitted thermionically, unaffected [16].

These discoveries quantitatively reinforced the difficulties in achieving stoichiometric distribution with this technique, as the varying kinetic energies, atomic mass, and valence states of the emitted species result in significantly different scattering cross-sections [4].

In order to combat the inherent non-stoichiometry of this technique, several deposition adjustments are often made. The distance between the target material and the substrate can be reduced to lessen the impact of the differing scattering cross-sections. The deposition pressure can also be increased in order to counteract lateral spreading through interaction with gas ambient. Lastly, the laser energy can be set just beyond the minimum for material emission. This ensures that the bimodal kinetic energy distribution, inherent to the ionic and neutral species, remains as low as possible [17].

2.4 Micromachined Ultrasonic Transducers

Micromachined ultrasonic transducers (MUTs) convert alternating currents into ultrasonic waves; they are utilized in a variety of high frequency applications. MUTs are categorized by the mechanism through which ultrasound is produced; the most common mechanisms are capacitive or piezoelectric.

2.4.1 Capacitive Micromachined Ultrasonic Transducers

In a capacitive micromachined ultrasonic transducer (cMUT), an applied DC bias deflects the flexible membrane towards the bottom plate. An applied AC voltage produces flexural oscillations of the membrane and generates ultrasound. **Figure 2.9** depicts the generic architecture of a cMUT cell.
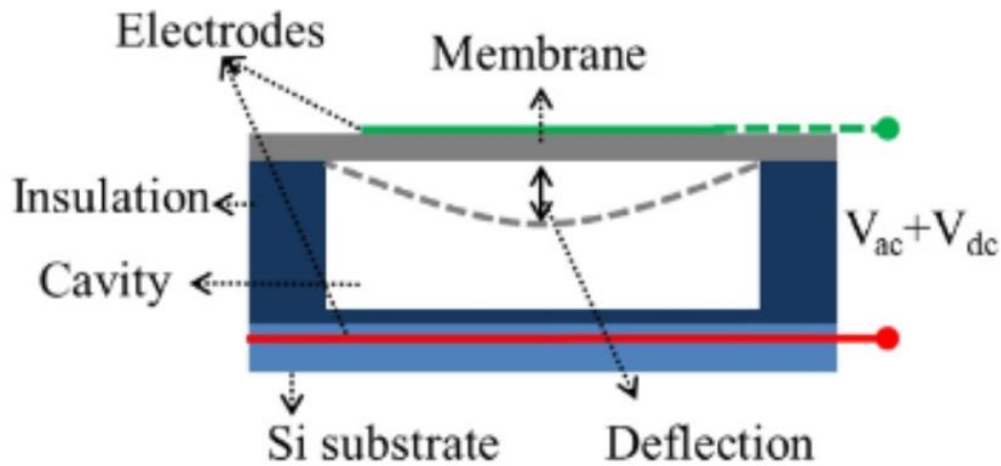
Figure 2.9: Schematic of the cMUT cell, adapted from [18]

cMUTs produce high bandwidths (up to 175%), high electromechanical coupling coefficients (~0.85), and high output acoustic pressure [19][20][21]. The operating frequency of a CMUT is dictated by the thickness of the flexural membrane, its lateral dimensions, and the elastic properties [22].

There are two main drawbacks of the cMUT cell. Their longevity is often poor as the DC bias near the collapse voltage of the CMUT cell driving high performance, increases the probability of failure. cMUTs are also difficult to manufacture, as 3D imaging and high frequency applications require thin, closely spaced transducer elements.

2.4.2 Piezoelectric Micromachined Ultrasonic Transducers

Piezoelectric micromachined ultrasonic transducers (pMUTs) operate through utilizing the converse piezoelectric effect with a thin-film piezoelectric material situated between two high conductivity electrode layers. The direct application of an AC voltage in the poling direction of the piezoelectric thin film actuates

flexural vibrations, producing ultrasonic waves. **Figure 2.10** depicts the generic architecture of a pMUT cell.
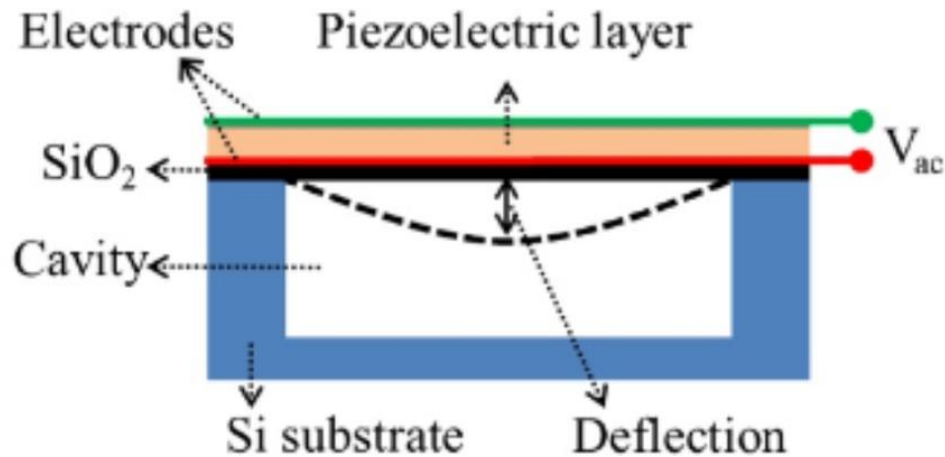
Figure 2.10: Schematic of the pMUT cell, adapted from [18]

The operating frequency of a pMUT can be controlled semi-independently of the piezoelectric layer thickness, through the dimensions and stiffnesses of the supporting materials, allowing easier design variations and manufacturing [22]. MUTs also offer the possibility to integrate the transducer and the ancillary electronics on the same device, possibly reducing signal noise and parasitic capacitance [22].

Chapter 3: Experimental Procedures

The synthesis of pulsed laser deposited $(K_{0.50}Na_{0.50})NbO_3$ (KNN) thin films consisted of three main components: the synthesis of the bulk ceramic target, the deposition of the KNN thin film, and post-deposition thermal annealing.

3.1 Bulk Ceramic Synthesis

The KNN bulk ceramic targets were synthesized using standard solid-state synthesis involving the reaction of potassium carbonate (K_2CO_3), sodium carbonate (Na_2CO_3), and niobium(V) oxide (Nb_2O_5) powder precursors at elevated temperatures, shown in the equation:

$$K_2CO_3(s) + Na_2CO_3(s) + 2Nb_2O_5(s) \rightarrow 4K_{0.5}Na_{0.5}NbO_3(s) + 2CO_2(g) \qquad \textbf{3.1}$$
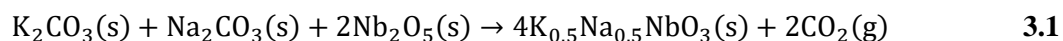
Calcination conditions were based on a Knudsen-effusion mass-spectrometry study suggesting that evacuating built up CO_2 gas and repeating the calcination steps would increase KNN formation [23]. Thus, the calcination of the KNN precursor powders was conducted using two discrete calcination steps with substantial intermediate milling before target sintering.

Potassium carbonate, sodium carbonate, and niobium(V) oxide powders were batched in the stoichiometric 1:1:2 ratio, then ball milled in ethanol using spherical stabilized zirconia media for 24 hours. The precursor powders were sourced shortly before the target synthesis, therefore it was assumed that a loss on ignition analysis was not required. The milled powder was placed in a crucible and partially covered with the crucible lid to allow evacuation of CO_2 without complete exposure to the furnace ambient. The powder was calcined for approximately 9 hours in total, using the profile detailed in **Table 3.1**. The calcination temperature range was selected on the basis of thermogravimetric analyses suggesting that the reaction should occur between 400 and 700°C [24].

Table 3.1: Calcination profile for bulk KNN target synthesis

Operation	Ramp Rate [°C/min]	Initial Temp. [°C]	Final Temp. [°C]	Duration [min]
Ramp	2	23	400	188.5
Hold	0	400	400	60
Ramp	3	400	700	100
Hold	0	700	700	60
Ramp	-5	700	23	135.5

The ideal weight loss of the KNN powder upon firing, indicating completion of the KNN reaction, assuming no evaporation of volatile species, is 12.8% based on **Equation 3.1**. The weight loss after the first calcination step was observed to be approximately 10%, suggesting significant decomposition of the initial powders.

Before the second calcination step, the KNN powder was batched with excess K_2CO_3 and Na_2CO_3 powders in a 2:1 ratio, to account for the volatilization of potassium and sodium during the pulsed laser deposition process. The excess powder added was determined in terms of the desired mole percentage of the KNN powder. Targets were synthesized with mole% excess compositional ratios of 10:5, 7.5:3.75, and 5:2.5 potassium carbonate to sodium carbonate. The effect of the varied %mole excess alkali content on the KNN thin film is discussed in **Section 4.2.1**.

The KNN powder with the added mole% excess was vibratory milled in ethanol using 1 cm diameter spherical stabilized zirconia media for 12 hours. The milled powder was placed in a crucible and partially covered with the crucible lid. The powder was calcined for approximately 9 hours in total using the profile detailed in **Table 3.1**, resulting in a second calcination step identical to the first.

The weight loss of the powder upon firing was observed to be approximately 11% of the added excess powder, indicating significant reaction. It is important to note that the weight loss upon firing for both calcination steps is increased by some volatilization of the alkali constituents.

The resulting KNN powder was pressed into 2-inch diameter targets using a Carver Model 30-12 (Carver Inc., Wabash, IN) hydraulic press. The targets were then vacuum sealed and compacted using an Autoclave Engineers (Erie, PA) cold isostatic press at 30,000 psi.

The target was sintered for approximately 16 hours in total using the profile detailed in **Table 3.2**.

Table 3.2: Sintering profile for bulk KNN target synthesis

Operation	Ramp Rate [°C/min]	Initial Temp. [°C]	Final Temp. [°C]	Duration [min]
Ramp	2	23	1075	526
Hold	0	1075	1075	240
Ramp	-5	1075	23	210.4

Sintering conditions were chosen to be below the KNN solidus temperature of 1140ºC [2][24]. 10:5 mole% excess targets were sintered at temperatures ranging from 1050 to 1150ºC to determine the optimum sintering temperature. The 10:5 mole% excess targets achieved the highest densification without melting at a sintering temperature of 1075ºC. The density of the ceramic targets was calculated from mass and dimension measurements, as seen in **Table 3.3**. The theoretical density of stoichiometric KNN is 4.51 g/cc [25].

Table 3.3: Densities of the sintered bulk KNN targets

%mole Excess [%K:%Na]	Density [g/cc]	%Theoretical Density
5:2.5	4.1	91
7.5:3.75	4.0	89
10:5	4.3	95

Further optimization can be done to obtain sintering temperatures for the 5:2.5 and 7.5:3.75 target compositions to yield a larger percentage of the theoretical density.

3.2 Pulsed Laser Film Deposition

Pulsed laser deposition was used to deposit $(K_{0.50}Na_{0.50})NbO_3$ (KNN) thin films on platinized silicon substrates in a custom-built PLD system, as illustrated in **Figure 3.1**.

3.2.1 System Description

a. KrF Excimer Laser
b. Plano-Convex Fused Silica Lens
c. K-type Thermocouple
d. Fused Quartz Laser Port
e. Baratron Capacitance
   Manometer
f. Hot-Stage Power Feedthrough
g. Ionization Pressure Gauge
h. Ferrofluidic Rotary
   Feedthrough
i. KNN Target
j. Stainless-Steel Hot-Stage
k. Turbomolecular Pump
l. Ozone Generator
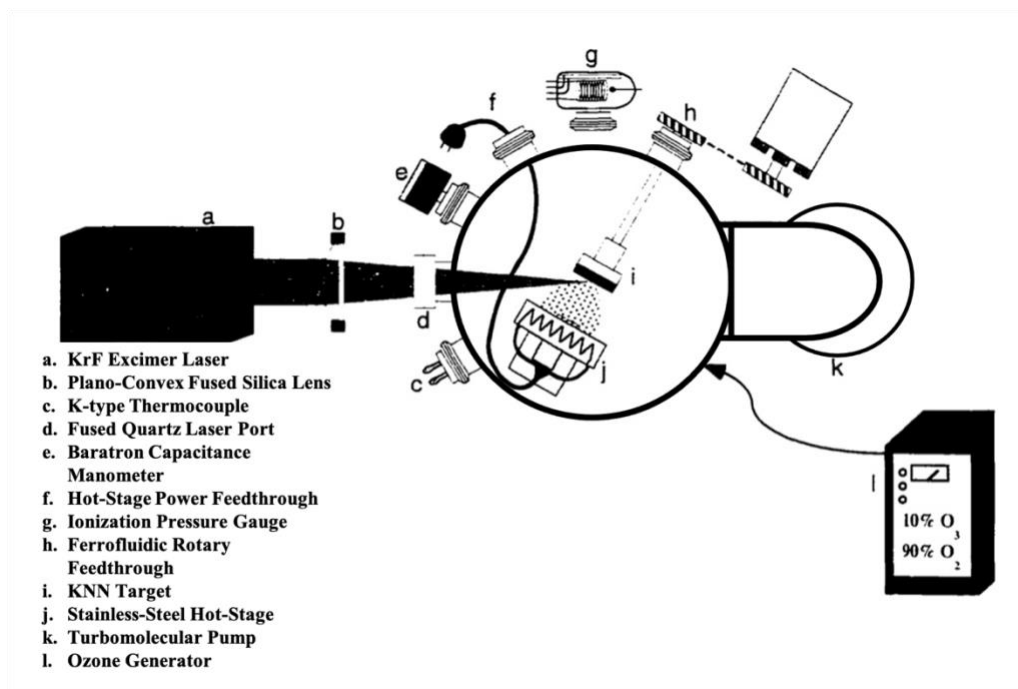
Figure 3.1: Schematic of the utilized pulsed laser deposition system, adapted from [4]

A COMPex 102 (Lambda Physik, Ft. Lauderdale, FL) KrF excimer laser was used to ablate the KNN targets. The laser was set to the constant energy mode with an energy output of approximately 185 mJ. The

duration of the laser pulses was approximately 30 ns, delivered at frequencies ranging from 5 to 20 Hz. The effects of varying the laser pulse frequency on the growth rate and volatility of the alkali species are discussed in **Section 4.2.2.1.3**. A plano-convex fused silica lens with a focal length of 0.5 m was used to focus the laser beam onto the KNN target. The position and orientation of the plano-convex lens was held constant through all depositions. The energy density was calculated to be 0.9 J/cm^2 using the set energy output and the area of a pulse delivered to the target measured through ablation of photosensitive film at the target surface.

The vacuum was achieved through the use of a TMP-1003LM (Shimadzu Corporation, Kyoto, Japan) turbomolecular pump, backed by an Edwards XDS 10 (Brook Crompton UK Limited, West Yorkshire, United Kingdom) scroll pump. The base ambient pressure of the chamber was $2 \cdot 10^{-7}$ Torr. Pressures higher than $5 \cdot 10^{-5}$ Torr were measured using an ionization pressure gauge. Pressures between $5 \cdot 10^{-5}$ Torr and 10^0 Torr were measured using a Baratron capacitance manometer.

The deposition ambient composition was 10% ozone and 90% oxygen supplied by a Model G-1 (PCI Ozone and Control Systems Inc., West Caldwell, NJ) ozone generator. The ozone/oxygen mixture was delivered to the chamber at a constant gas flow rate of approximately 26 cm^3/min.

The substrates were affixed to a stainless-steel hot stage using silver thermal paste (Alfa Aesar, Haverhill, MA), resistively heated using a variable temperature AC controller.

The KNN bulk ceramic targets were mounted to a ferrofluidic rotary feedthrough, rotating at approximately 1-2 rpm during deposition. This helped utilize the target surface more uniformly.

3.2.2 Substrate Preparation

The KNN thin films were deposited onto platinized silicon wafers, purchased from NOVA Electronic Materials LLC. The depth profile of the platinized silicon wafers is detailed in **Table 3.4** and shown in **Figure 3.2**.

Table 3.4: Layer composition of the platinized silicon wafers (NOVA Electronic Materials LLC, Flower Mound, TX)

Layer	Thickness
Pt	150 nm
Ti	20 nm
SiO_2	1 µm
Si	500 µm
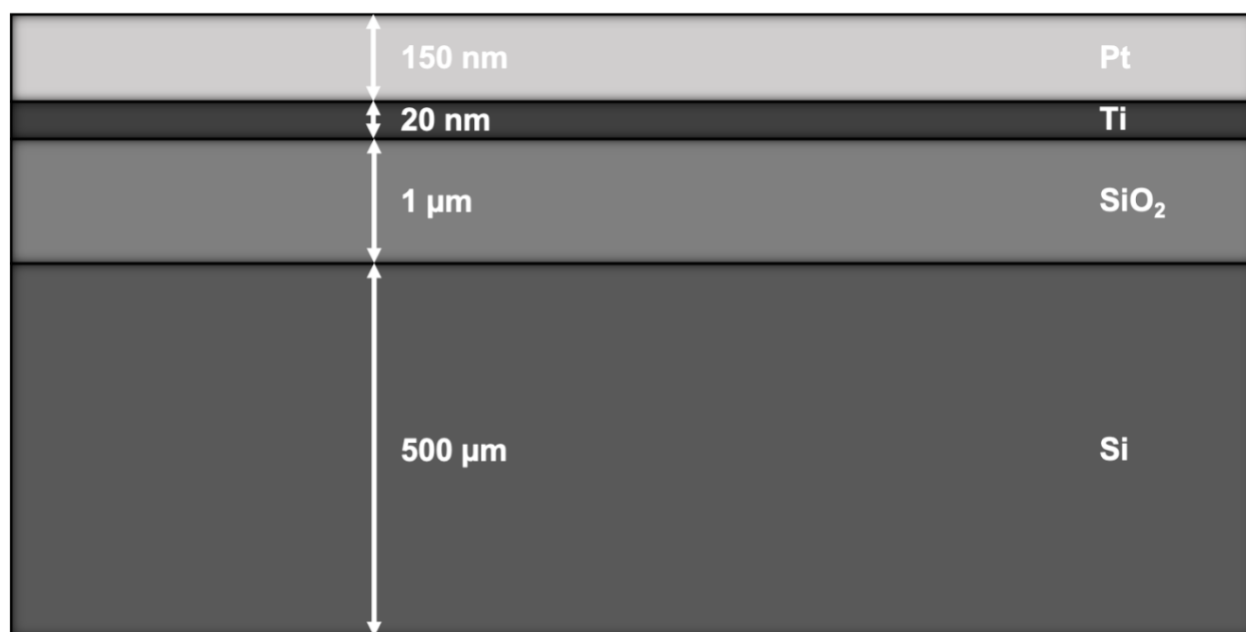
Figure 3.2: Cross-sectional diagram of platinized silicon wafer (NOVA Electronic Materials LLC, Flower Mound, TX), {not to scale}

To prepare the platinized silicon substrates for deposition, the wafer was first manually cleaved into a 1 cm^2 square substrate by applying pressure with a diamond scribe along the (111) cleavage plane of single crystal silicon. The substrate was then cleaned through a sequential series of approximately 5-minute ultrasonication steps in acetone, ethanol, and isopropyl alcohol. The clean substrate was adhered to the hot stage using silver thermal paste cured with a temperature ramp to 300°C for 1.5 hours.

3.2.3 Target Preparation

The KNN targets were stored in a box furnace set to 137°C until use to reduce exposure to atmospheric moisture. To prepare the KNN target for deposition, the target was first wet-polished in isopropyl alcohol with a sequential series of 180-grit and 400-grit silicon carbide sandpaper to remove surface defects from previous depositions. The polished target was returned to the 137°C box furnace for approximately 10 minutes to assure volatilization of the isopropyl alcohol.

Pre-ablation was performed to prepare the target surface for deposition. The bulk KNN target was placed on the ferrofluidic rotary feedthrough in the deposition chamber, and manually aligned with the KrF excimer laser. Pre-ablation was performed on the surface of the bulk KNN target with the parameters detailed in **Table 3.5**.

Table 3.5: Bulk KNN target pulsed laser pre-ablation parameters

Parameter	Set Point
Pulse Rate	20 Hz
Ambient Pressure	760 Torr
Duration	60 s

3.2.4 Chamber Preparation

The stainless-steel hot stage, with the bonded platinized silicon substrate, was placed in the deposition chamber and aligned to the pre-ablated bulk KNN target with a custom alignment tool. The distance between the platinized silicon substrate and the bulk KNN target (target-to-substrate distance) was varied over the range of 4 to 7 cm to directly affect the kinetic energies of the emitted species upon bombardment with the substrate surface. The effect of the variation of the target-to-substrate distance on the microstructure and phase purity of the deposited KNN films is discussed in **Section 4.2.2.1.2**.

The deposition chamber was then set to pump down to base ambient pressure ($2 \cdot 10^{-7}$ Torr), however, in many cases, a chamber ambient pressure of less than $1 \cdot 10^{-6}$ Torr was used prior to deposition as the system would take approximately 3 hours to reach $1 \cdot 10^{-6}$ Torr, compared to approximately 20 hours to reach base ambient pressure.

3.2.5 Deposition Ambient Preparation

Upon reaching a suitable base ambient pressure, the TMP-1003LM turbomolecular pump was reduced to 25% of the maximum speed to allow for increased chamber pressure. The Model G-1 ozone generator was turned on and the valve connecting the Model G-1 output to the system chamber was opened. The chamber ambient pressure was observed until the deposition ambient pressure, which was varied from 100 to 400 mTorr, was reached through systematic, manual adjusting of the gate valve to the TMP-1003LM turbomolecular pump. The effects of the varied deposition ambient pressure on the stoichiometric control and energetic bombardment of the ionic species, and therefore the phase purity and microstructure of the KNN thin film, are discussed in **Section 4.2.2.1.2**.

3.2.6 Deposition

Upon successful preparation of the deposition ambient, the stainless-steel hot stage was set to ramp to deposition substrate temperature. The substrate temperature was varied from 450 to 800°C to directly affect the adatom mobility of the atoms during deposition. The effect of varying the substrate temperature on the microstructure of the KNN thin film and its relation to the structure zone model are discussed in **Section 4.2.2.1.1**.

Upon stable deposition ambient and substrate temperature, the ferrofluidic rotary feedthrough for target rotation and the KrF excimer laser were activated. After the elapsed deposition duration, which was varied from 5 to 20 minutes, the heated stainless-steel hot stage and the COMPex 102 KrF excimer laser were simultaneously deactivated, the gate valve to the TMP-1003LM turbomolecular pump was closed, and the valve to the Model G-1 ozone generator was closed. The effect of the varied deposition time on the thickness of the KNN thin film is discussed in **Section 4.4.2.1.3**. The aforementioned operations immediately following deposition completion were performed in quick succession to assure the cooling ambient was as identical to the deposition ambient as possible.

3.2.7 Sample Cooling and Removal

The cooling ambient pressure was maintained until the substrate temperature dropped below 100°C, then the chamber was vented through the opening of a ventilation valve until atmospheric pressure was reached. The KNN target was returned to the 137°C furnace. The stainless-steel hot stage was removed from the system, and the substrate with the deposited KNN thin film was carefully separated from the substrate heater and stored in a sample holder.

3.3 Thermal Annealing

The KNN thin films were thermally annealed in an RTP 600s (Modular Process Technology, San Jose, CA) rapid thermal processing system. The samples were placed film-side up in the RTP, then the annealing profile was selected. The samples were annealed in N_2. The annealing temperatures were varied from 700°C to 800°C based on the range of the ratio of substrate temperature to melting temperature, identified by the structure zone model, that promotes surface diffusion, as discussed in **Section 4.2.2.1.1**. The annealing duration was varied from 5 to 10 minutes, based on an initial arbitrary selection due to conflicting suggestions from literature, then modified based on characterization results. The effects of varying the annealing temperature and duration on the modification of film microstructure and phase purity are discussed in **Section 4.2.3.** The annealing profile is detailed in **Table 3.6.**

Table 3.6: Post-deposition thermal annealing profile

Operation	Initial Temp. [°C]	Final Temp. [°C]	Duration [min]
Ramp	23	400	0.25
Hold	400	400	0.5
Ramp	400	Varied	0.25
Hold	Varied	Varied	Varied
Ramp	Varied	200	~2

The system was untouched until the temperature reached 200°C, then the RTP was opened. Upon the sample temperature reaching 100°C, the sample was then returned to the sample holder.

Chapter 4: Results and Discussion

Several KNN thin films, spanning extensive parameter variation as seen in **Table 4.1, 4.2** and **4.3**, were successfully synthesized through the pulsed laser deposition process, as detailed in **Chapter 3**, and subjected to material characterization. A complete parameter breakdown of every completed deposition is documented in **Appendix A**.

Table 4.1: Varied bulk KNN target composition parameters

Composition Parameter	Set Points
Excess K:Na [mole%]	10:5, 7.5:3.75, 5:2.5

Table 4.2: Varied pulsed laser deposition parameters

Deposition Parameter	Set Points
Target-to-Substrate Distance [cm]	2.0, 2.5, 4.0, 5.0, 5.1, 5.3, 5.7, 6.0, 7.0
Deposition Pressure [mTorr]	100, 200, 300, 400, 500
Temperature [$^{\circ}$C]	450, 550, 600, 650, 675, 700
Repetition Rate [Hz]	5, 10, 15, 20
Duration [min]	5, 6, 7, 10, 20

Table 4.3: Varied thermal annealing parameters

Anneal Parameter	Set Points
Temperature [$^{\circ}$C]	700, 750, 800
Duration [min]	5, 10

The results of this study will be used to provide a basis for the further improvement of the KNN pulsed laser deposition process. As such, this chapter not only details the synthesis parameters, phase and microstructure analysis, and electrical performance for the highest achieved quality of synthesized KNN

thin films, but more importantly explores the learnings from varying the synthesis parameters to propose, in **Section 6.1**, future adjustments to promote successful utilization in pMUTs.

4.1 Resultant KNN Thin Film

Upon the completion of this study, the synthesis conditions producing the phase pure KNN thin film upon which future optimization will be based, were grown with the constant parameters detailed in **Chapter 3**, with additional details as follows. The bulk ceramic target of $(K_{0.50}Na_{0.50})NbO_3$ contained 5 mole% excess potassium and 2.5 mole% excess sodium, sintered to a density of 4.1 g/cc. The platinized silicon substrate was aligned to the KNN target at a target-to-substrate distance of 5.7 cm. The deposition ambient reached a base pressure of $2.2 \cdot 10^{-7}$ Torr before being increased to a deposition ambient pressure of 400 mTorr. The substrate temperature was set to 550°C and the pulse rate of the excimer laser was set to 5 Hz for a deposition duration of 6 minutes. The substrate was allowed to cool to room temperature at a cooling ambient pressure of 400 mTorr before thermal annealing at 700°C for 5 minutes. The complete parameter breakdown for the optimized KNN thin film is detailed in **Table 4.4, 4.5,** and **4.6**.

Table 4.4: Bulk KNN target composition parameters for resultant film

Composition Parameter	Set Point
Target mole% Excess K:Na	5:2.5
Target Density	4.1 g/cc
Substrate	Platinized Silicon (NOVA Electronic Materials, LLC, Flower Mound, TX)

Table 4.5: Pulsed laser deposition parameters for resultant film

Deposition Parameter	Set Point
Target-to-Substrate Distance	5.7 cm
Deposition Ambient Composition	10% O_3, 90% O_2
Base Ambient Pressure	$2.2 \cdot 10^{-7}$ Torr
Deposition Ambient Pressure	400 mTorr
Substrate Temperature	550ºC
Energy Density	0.9 mJ/cm^2
Pulse Rate	5 Hz
Pulse Duration	30 ns
Deposition Duration	6 min

Table 4.6: Thermal annealing parameters for resultant film

Anneal Parameter	Set Point
Temperature	700ºC
Anneal Duration	5 min

4.1.1 Perovskite Phase Analysis

X-ray powder diffraction (XRD) was used to assess the perovskite phase-purity and crystal orientation of the KNN thin films. XRD plots were obtained via an X'Pert PRO MPD (PANalytical Inc., Alemo, The Netherlands) x-ray diffractometer. The x-ray diffraction scan parameters are shown in **Table 4.7**. The resultant data were analyzed and processed with Jade Complete XRD Analysis and OriginPro software respectively.

Table 4.7: X-ray diffraction scan parameters (X'Pert PRO MPD, PANalytical Inc., Alemo, The Netherlands)

Parameter	Set Point
Mask	10 mm
2θ Range	10° to 70°
Scan Rate	0.067°/s
Scatter Slit	1/2°
Current	50 mA
Voltage	45 kV

Figure 4.1 and Figure 4.2 show the XRD patterns for the optimized $(K_{0.50}Na_{0.50})NbO_3$ thin film deposited through pulsed laser deposition in this study, and a high-quality $(K_{0.50}Na_{0.50})NbO_3$ thin film deposited through RF magnetron sputtering by Shibata et al. [26], both deposited on platinized silicon substrates.
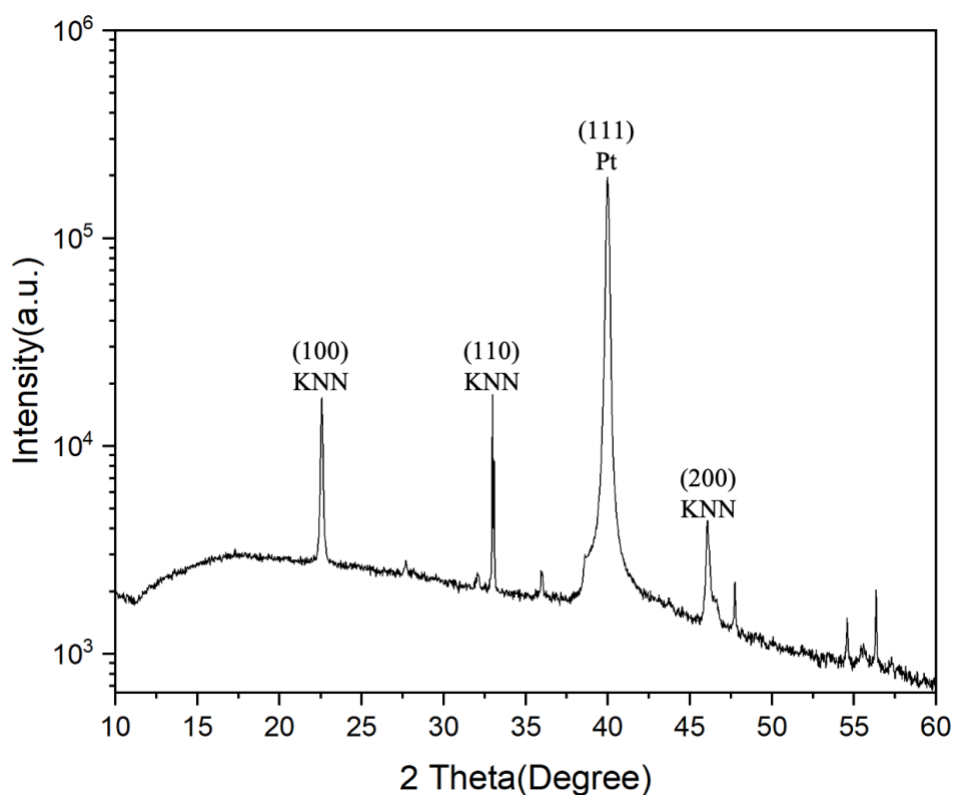
Figure 4.1: XRD pattern for resultant KNN thin film
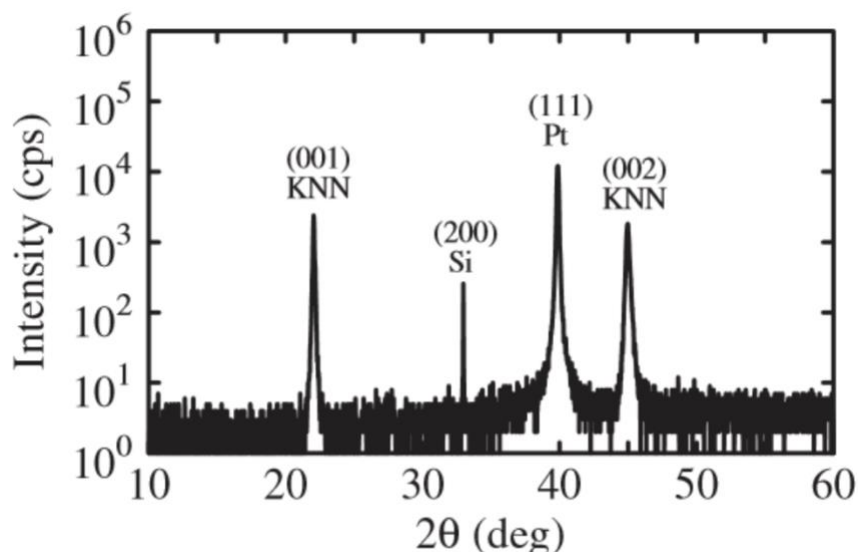
Figure 4.2: XRD pattern for KNN thin film deposited by Shibata et al., taken from [26]

The XRD patterns indicate that both films contain strong perovskite structure with minimal secondary phases. A key distinction between the XRD spectra can be made, however. The KNN film deposited in this study returned an almost even split in the intensity of the peaks arising from the (100) and (110) planes, while the KNN film deposited by Shibata et al. returned a perfect (001) perovskite orientation. The incomplete texture of the films produced in this thesis has significant ramifications to the electrical performance of the KNN thin film.

4.1.2 Thin Film Microstructure

Scanning electron microscopy (SEM) was used to assess the morphology of the KNN thin films. Images were taken using Merlin (Carl Zeiss Microscopy GmbH, Jena, Germany), GeminiSEM 500 (Carl Zeiss Microscopy GmbH, Jena, Germany), and Apreo (Thermo Fisher Scientific, Waltham, MA) field emission scanning electron microscopes (FESEMs). The SEM imaging parameters are shown in **Table 4.8**. The voltage, current, and working distance parameters were varied to produce optimal images. Samples were electrically grounded using Cu tape to increase image quality by reducing charging.

Table 4.8: SEM imaging parameters. Merlin (Carl Zeiss Microscopy GmbH, Jena, Germany), GeminiSEM 500 (Carl Zeiss Microscopy GmbH, Jena, Germany), Apreo (Thermo Fisher Scientific, Waltham, MA)

Parameter	Set Point
Imaging Mode	Secondary Electrons
Merlin	InLens
GeminiSEM	InLens
Apreo	Immersion T2
Voltage	1.00, 3.00, 5.00 kV
Current	13, 25, 50 pA
Working Distance	2.3 to 3.9 mm

Figures 4.3 and **4.4** show the SEM cross-sectional images for the optimized $(K_{0.50}Na_{0.50})NbO_3$ thin film deposited through pulsed laser deposition in this study, and a high-quality $(K_{0.50}Na_{0.50})NbO_3$ thin film deposited through RF magnetron sputtering by Shibata et al. [26], both deposited on platinized silicon substrates.
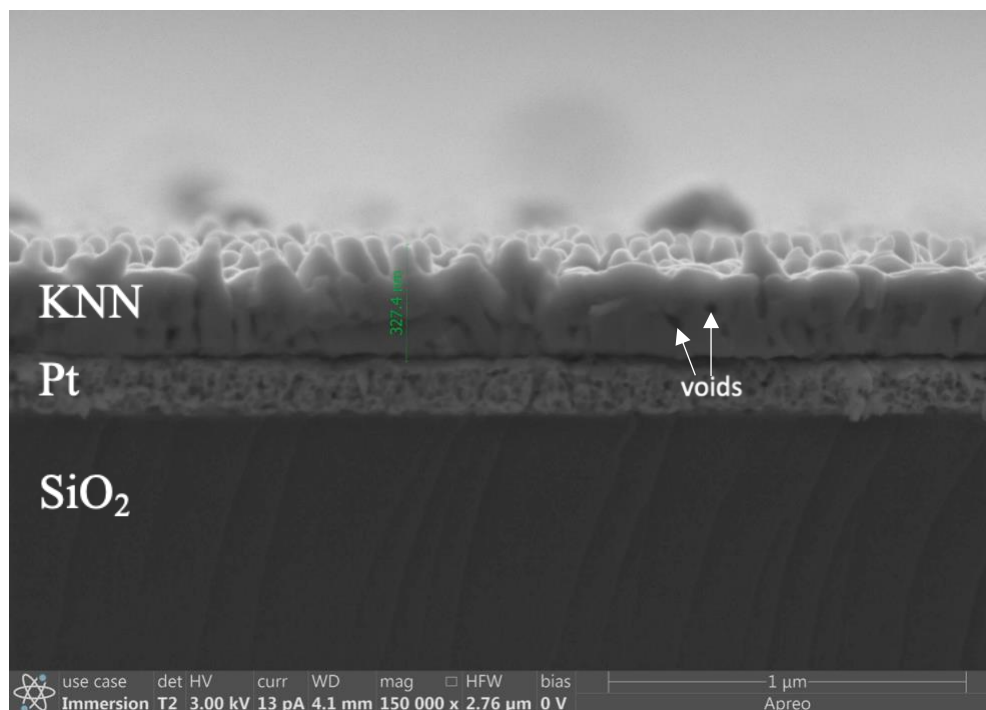
Figure 4.3: SEM cross-section of resultant KNN thin film
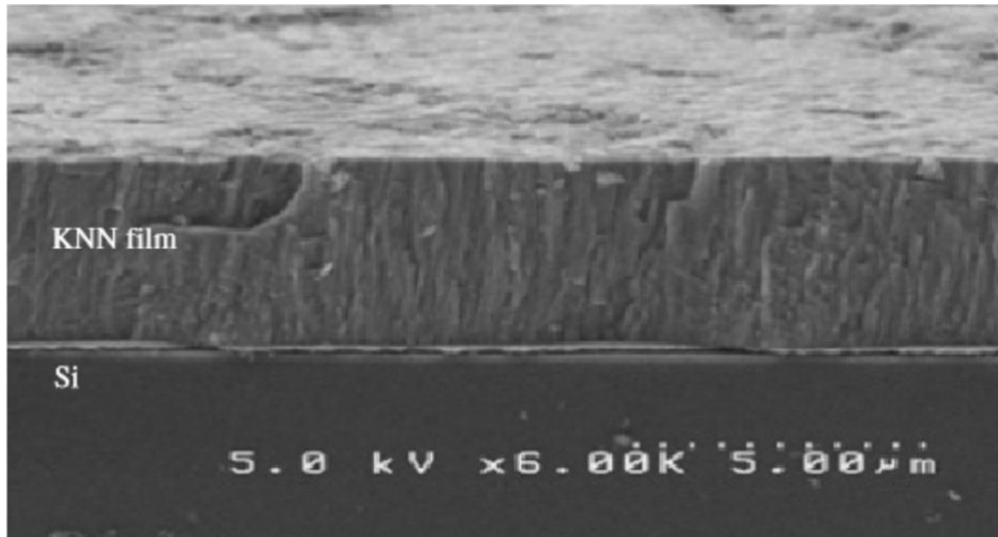
Figure 4.4: SEM cross-section of KNN thin film, taken from [26]

The microstructure of the two KNN thin films are very different. The thin film synthesized by Shibata et al.[26] exhibits a nearly perfect microstructure consisting of dense columnar grains culminating in a smooth surface, characteristics that predict strong piezoelectric performance and the possibility of a high dielectric breakdown strength [5][6]. The thin film synthesized in this study however, exhibited a microstructure containing several voids and high surface roughness, characteristics that do not suggest strong piezoelectric performance [3,26]. The reasoning behind the nature of this microstructure and its formation is discussed in **Section 4.2.**

4.1.3 Electrical Performance

Electrical measurements were taken on a custom-built probe station featuring a Precision Multiferroic (Radiant Technology Inc., Albuquerque, NM) materials analyzer. A P-E hysteresis loop was obtained for the ~300 nm thick thin film using the parameters shown in **Table 4.9**.

Table 4.9: Parameters for P–E measurement (Precision Multiferroic, Radiant Technology Inc., Albuquerque, NM)

Parameter	Set Point
Sample Area	$1.96*10^{-3}$ cm^2
Sample Thickness	300 nm
Field	150 kV/cm
Frequency	10 kHz
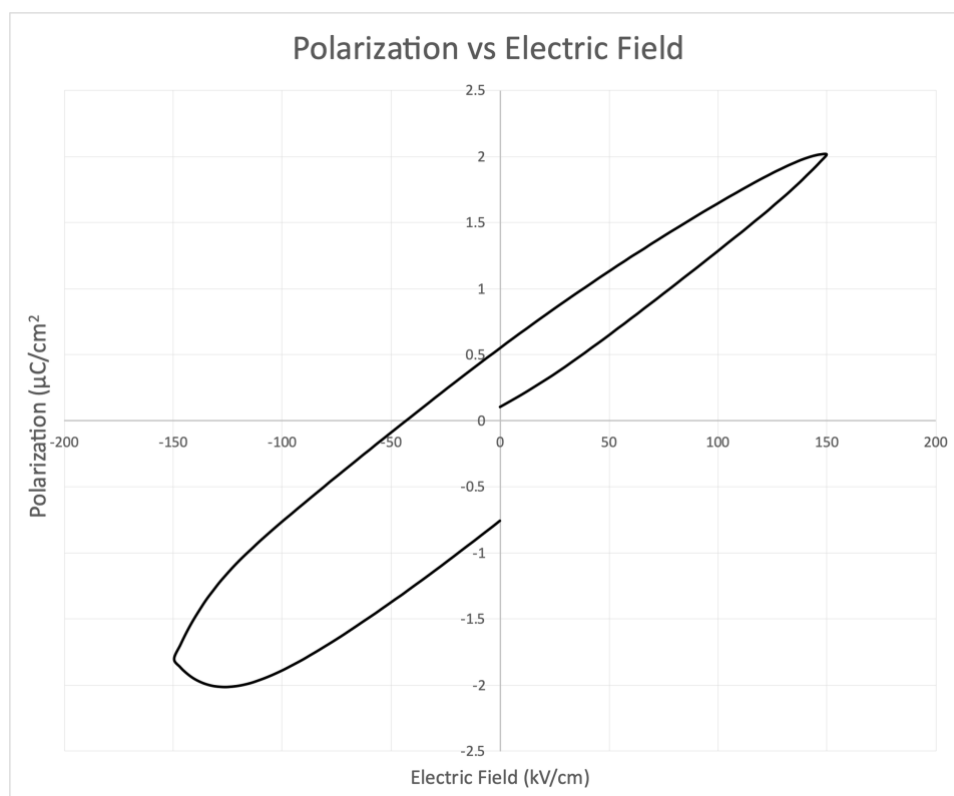
Figure 4.5: Polarization-electric field hysteresis loop for KNN thin film of interest

The characterization of the KNN thin film shows poor results, with high levels of conductivity. It is possible that the high leakage current density was produced by a high concentration of h$^+$ carriers induced by alkali deficiencies.

The remanent polarization (P_r) of the thin film was determined using a PUND (Positive Up Negative Down) measurement at the parameters detailed in **Table 4.10**.

Table 4.10: Parameters for PUND measurement (Precision Multiferroic, Radiant Technology Inc., Albuquerque, NM)

Parameter	Set Point
Sample Area	$1.96*10^{-3}$ cm^2
Sample Thickness	300 nm
Field	200 kV/cm
Pulse Delay	10 ms
Pulse Width	0.1 ms

The remanent polarization was measured to be 10.7 µC/cm^2 . The maximum polarization (P) was measured

to be 12.7 µC/cm^2.

The dielectric constant of the film was determined using the equation;

$$P = \varepsilon_0 \chi_e E = \varepsilon_0 (\varepsilon_r - 1)E \qquad\qquad \textbf{4.1}$$

where χ_e is the electric susceptibility, ε_r is the dielectric constant, ε_0 is the permittivity of free space, E is

electric field. The dielectric constant was determined to be 606. The loss tangent was measured to be 2.8%.

Section 4.2 discusses the optimization of the synthesis process that led to the observed phase purity,

microstructure, electrical performance of the concluding KNN thin film, while **Section 6.1** details further

improvements to increase piezoelectric performance.

4.2 Synthesis Parameter Analyses

The synthesis of KNN thin films consisted of three main components: the synthesis of the bulk ceramic

target, the pulsed laser deposition of the KNN thin film, and the thermal annealing of the KNN thin film.

As such, this section is divided into three sub-sections, each detailing the rationale and influence of the

parameters varied for each synthesis component.

4.2.1 Bulk KNN Target Composition

High performance pMUTs require uniform and stoichiometric thin films. Due to the considerable macroparticulate generation and non-stoichiometry characteristic of the pulsed laser deposition technique, as discussed in **Section 2.3.2**, the two main compositional parameters that affect the quality of the KNN thin film are the target's density and excess alkali content.

A bulk KNN target for pulsed laser deposition must be highly dense to reduce the effect of target porosity generating copious ejection of macroparticulates [4][27]. The solid-state synthesis process used in this study, outlined in **Section 3.1.1**, produced sintered bulk KNN targets of high enough density ($\gtrsim$ 90% theoretical density) that the effect of the difference in porosity between targets would be minimal, and not produce target-induced deviations in quality of the thin film.

A bulk KNN target for pulsed laser deposition must also incorporate excess alkali content for two separate reasons. The first is the consequence of pulsed laser deposition resulting in the increased scattering of lighter species upon laser ablation. A compositional distribution analysis of the ejected plasma plume shown in **Figure 2.7** would show higher concentrations of the heavy cations, Nb^{5+}, towards the center region of the plasma plume, and higher concentrations of the lighter cations, K^+ and Na^+, towards the outer regions of the plasma plume. However, due to the deposition optimization performed in this study, discussed in detail in **Section 4.2.2.1.2**, it is speculated that the effect of cation scattering was minimal for the deposited thin films of interest.

The second reason concerns the volatility of potassium and sodium at elevated temperatures. Films deposited from a ceramic target with inadequate excess potassium and sodium would exhibit deficiencies in the stoichiometry of the film, affecting the electrical performance. Unfortunately, due to covid-19 induced laboratory closures, it was not possible to assess depositions from all of the targets made. Thus, in this thesis, the subsequent pulsed laser depositions were conducted with a KNN bulk target with the following excess alkali percentages: 5% K, 2.5% Na.

4.2.2 Pulsed Laser Deposition Parameters

To determine the methodology of varying the pulsed laser deposition parameters, it was important to consider how each variable affects the formation of the thin film. This section discusses the process of thin film formation, the material interactions that dictate the formation phenomena, and how these phenomena are influenced by the parameters of pulsed laser deposition.

4.2.2.1 Thin Film Formation Analysis

Thin film formation through physical vapor deposition techniques can be ordered into three sequential steps predicated on the movement of the depositing material: the transport of the ablated species to the substrate through the deposition ambient, the adsorption and surface diffusion of adatoms across the substrate, and the chemical reaction and bulk diffusion of the adatoms resulting in either incorporation into the growing structure or desorption from the surface [28].

The deposition parameters that affect the transport of the ablated species include: the energy density dictating the initial velocity and kinetic energy, the pulse duration which was set by the manufacturer of the laser, the deposition ambient composition introducing chemical interaction, the deposition ambient pressure affecting mechanical interaction and mean free path, and the target-to-substrate distance affecting the bombardment energy [4][29][28][30]. The deposition parameter that most directly affects the adsorption and surface diffusion of the atoms is the substrate temperature, dictating the adatom mobility at grain surfaces and interfaces [30]. The deposition parameter that most directly affects the chemical reaction and bulk diffusion of the adatoms is also the substrate temperature, dictating the adatom mobility through the grain volume and influencing adatom desorption [30][26].

To further understand the formation kinetics of thin films, film formation can also be classified into three phenomena predicated on the kinetic interactions of the bombarding species, film, and substrate material

[4][30]. The first of these is nucleation, or the condensation of the bombarding atoms into crystal nuclei on the substrate surface. Nucleation is determined by the relative interaction energies of the bombarding, film, and substrate atoms. The second phenomenon is coalescence, or the growth of nuclei until formation of a continuous network. Coalescence is dictated by the film surface energies, the vapor pressure of the bombarding material, and the equilibrium vapor pressure of the substrate material. The last of the three is the film thickness growth, affected by the number of pulses and the adatom mobility; the growth rate is dictated by the pulse rate and the adatom mobility. It is important to note that the thickness and growth rate are not consistently related to the aforementioned parameters during all stages of the formation process; the observed growth rates of the KNN thin films are discussed in more detail in **Section 4.2.2.1.3**.

Given the complexity of the interactions and the number of possible variations, the methodology of which parameters to vary was hence determined based on the magnitude of the effect and the ease of the variation. As such, parameters with a comparatively minimal effect on the film formation, including the gas flow rate and the cooling ambient pressure, and those that were challenging to accurately control, including the energy density and pulse duration, were kept largely constant throughout the study.

The first goal of this study was to obtain films with high perovskite crystallization without the presence of secondary phases. The second goal was to achieve with an optimal microstructure consisting of dense, columnar grains, a smooth surface, and optimal defect chemistry. These thin film characteristics would predict the strongest piezoelectric properties obtainable for KNN.

Sections 4.2.2.1.1, 4.2.2.1.2, and 4.2.2.1.3 discuss the varied deposition parameters, analyze the variation results, and present the findings and shortcomings of the work.

4.2.2.1.1 Effect of Substrate Temperature

The substrate temperature is perhaps the largest single determinant of the structure of a thin film, affecting all three kinetic interaction phenomena, and therefore was the first varied deposition parameter in this study.

For almost all thin films, the diffusion characteristics can be classified based on the relation of the substrate temperature to the material melting temperature, by a concept known as the structure zone model illustrated in **Figure 4.7**.
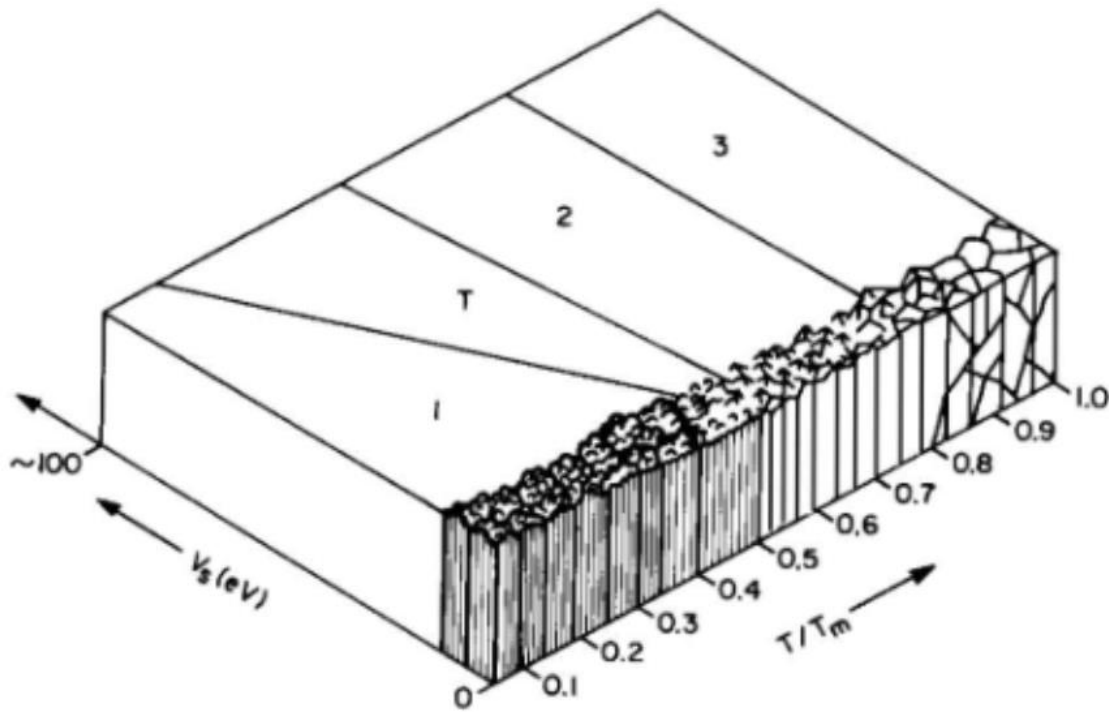
Figure 4.6: Structure zone model for thick films showing the effects of both bombardment and thermal-induced mobility, adapted from [31]

The structure zone model adapted for the thin film physical structure presents four regions (based on temperature in Kelvin) where T_S is the substrate temperature and T_m is the material melting temperature:

- Zone I ($T_s/T_m < 0.5$): Bombardment dominates, resulting in porous fine-grains

- Zone T (Subset of Zone I): Low surface diffusion resulting in blend between Zone I and Zone II structures

- Zone II ($0.5 < T_s/T_m < 0.75$): Surface diffusion dominates resulting in columnar grains

- Zone III ($T_s/T_m > 0.75$): Bulk diffusion dominates resulting in equiaxed grains

Interpreting the structure zone model, utilizing the solidus temperature of KNN without correction for bombardment induced mobility, presents the following three approximate regions:

- Zone I: $T_s \lesssim 435°C$

- Zone II: $435°C \lesssim T_s \lesssim 785°C$

- Zone III: $T_s \gtrsim 785°C$

It is important to note that these regions are based on solidus temperature, i.e., the minimum temperature at which the solid solution exhibits melting.

Analysis of the structure zone model, in reference to the microstructural characteristics that promote high piezoelectric response, determined a target of Zone II growth, and thus a substrate temperature range roughly between 400°C and 800°C. **Figure 4.8** shows the XRD patterns for initial depositions performed at 550°C, 600°C, 650°C, and 700°C.
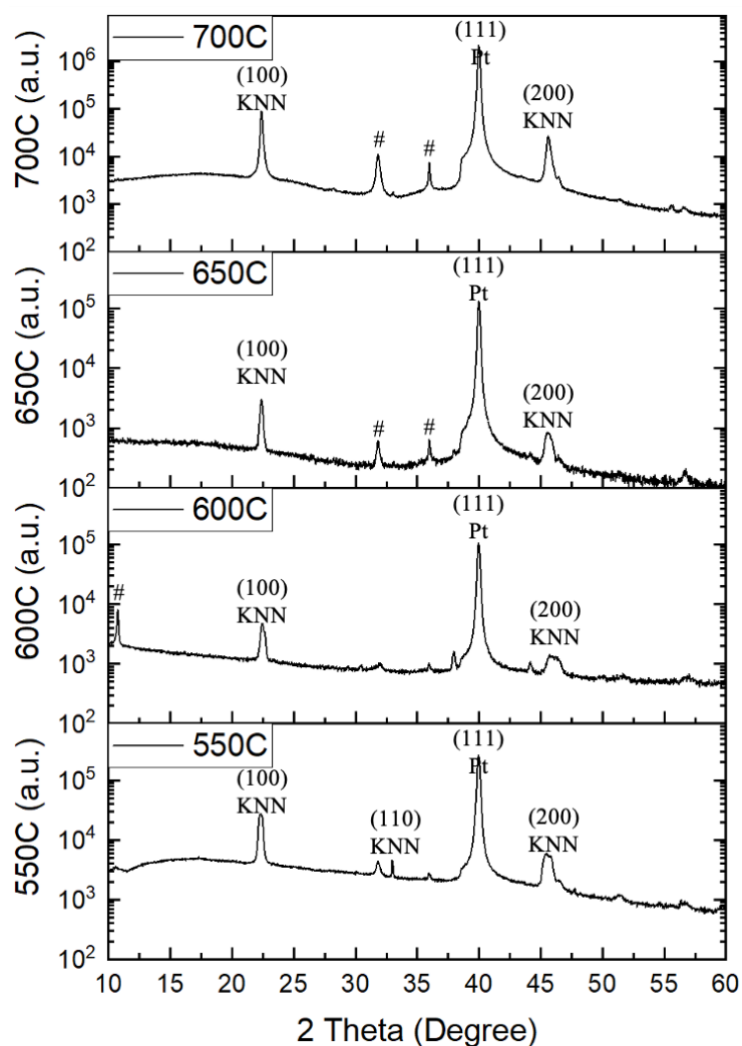
Figure 4.7: XRD patterns for depositions conducted at 550ºC, 600ºC, 650ºC, and 700ºC

Based on a comparison of the strengths of the perovskite peaks and presence of secondary phases, a substrate temperature of 650ºC was initially selected for further deposition parameter optimization.

Further analysis of the effect of the substrate temperature on the microstructure and phase purity of the thin films was conducted following the subsequent deposition parameter optimization. Due to other deposition parameters affecting the growth of the thin film, these effects are described in reference to those parameters, and are detailed in **Section 4.2.3**.

4.2.2.1.2 Effect of Deposition Ambient Pressure and Target-to-Substrate Distance

Following the initial variation of substrate temperature, the deposition ambient pressure and target-to-substrate distance was investigated to promote phase pure film deposition. The deposition ambient pressure is directly related to the frequency of collisions in the emitted plasma plume, in other words, the mean free path of the emitted species [4]. Therefore, as the emitted species propagate through the gas phase, their kinetic energies decrease through collision thermalization, resulting in strongly coupled effects of the deposition ambient pressure and target-to-substrate distance on the bombardment energy of the emitted species [4].

Based on this coupling effect, and a theoretical optimum bombardment energy range for Zone II growth at a given substrate temperature, it is reasonable to speculate that for a given deposition ambient pressure there exists a specified target-to-substrate distance at which the optimum bombardment energy occurs. To evaluate this conjecture, the emitted brilliant plasma plume was observed at set deposition ambient pressures, without the presence of a substrate, to quantitatively analyze the coupling effect. **Figure 4.9** shows the images of this analysis conducted at 100, 200, 300, and 400 mTorr.
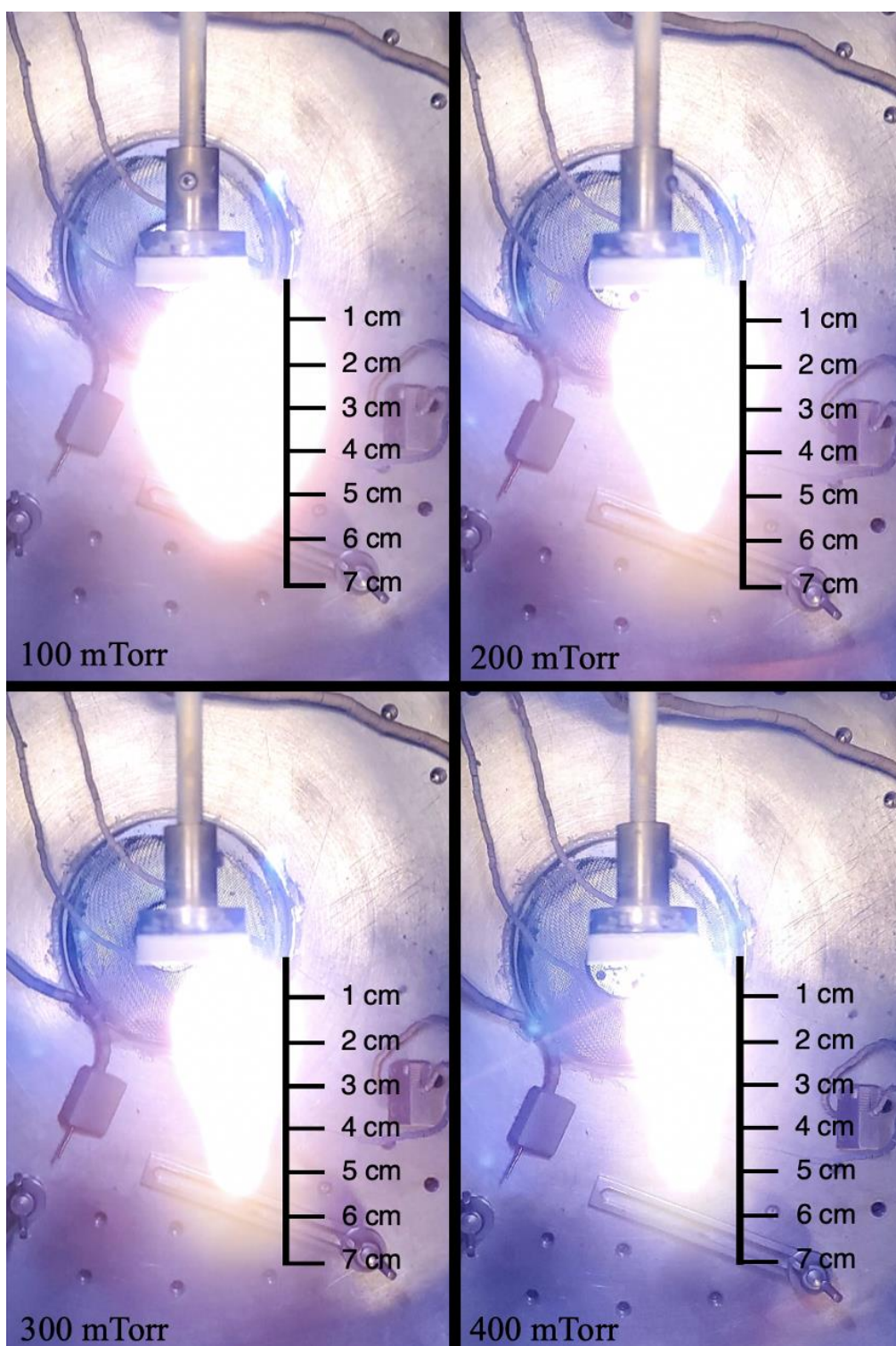
Figure 4.8: Deposition ambient pressure effect on emitted brilliant plasma plume

This experiment clearly demonstrated the constriction of both the lateral and distal spreading of the brilliant plasma plume with increasing deposition ambient pressure. Based on the results of this analysis and that for optimum film growth, the bombarding species must be of sufficient energy to initiate surface interaction without subsurface damage [4][17], a hypothesis was formulated that the optimum species bombardment energy, for a given deposition ambient pressure, was achieved at the tip of the brilliant plasma plume.

To evaluate this hypothesis, a series of depositions were performed in which the deposition ambient pressure and target-to-substrate distance were varied. For each deposition ambient pressure, a deposition was performed at three separate target-to-substrate distances corresponding in reference to the substrate's physical location in the brilliant plasma plume: substantially inside the plume, outside the plume, and where the edges of the substrate are just within the tip of plume.

Figure 4.10 and **4.11** depict a comparison of the XRD patterns visualizing the conclusions of this experiment. **Figure 4.10** shows the XRD patterns for the depositions conducted where the substrate was located just within the tip of the brilliant plasma plume for each deposition ambient pressure.
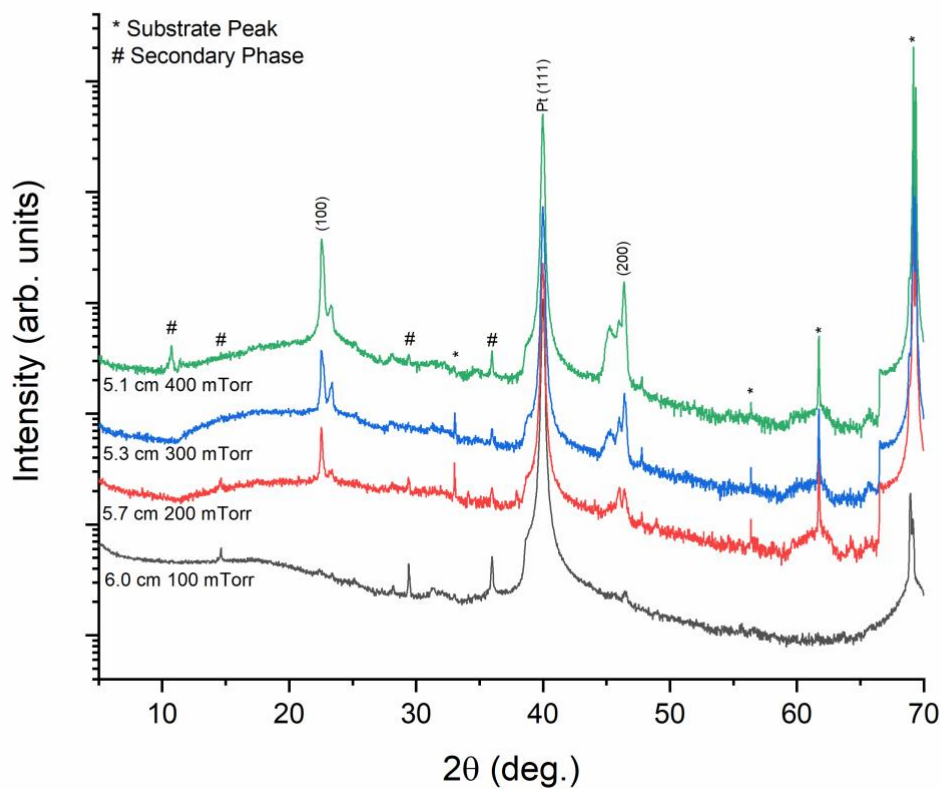
Figure 4.9: XRD patterns for depositions conducted at a target-to-substrate distance just within the tip of the brilliant plasma plume

The strength of the perovskite peak intensified with increasing deposition ambient pressure, possibly indicating improved crystallization of the perovskite phase (as larger deposition pressures could result in thicker films returning stronger peaks). However, the presence of secondary phases also increased with increasing deposition pressure. This target-to-substrate location, just within the tip of the brilliant plasma plume, resulted in the most phase pure films, when compared to the two other analyzed location, at each deposition ambient pressure.
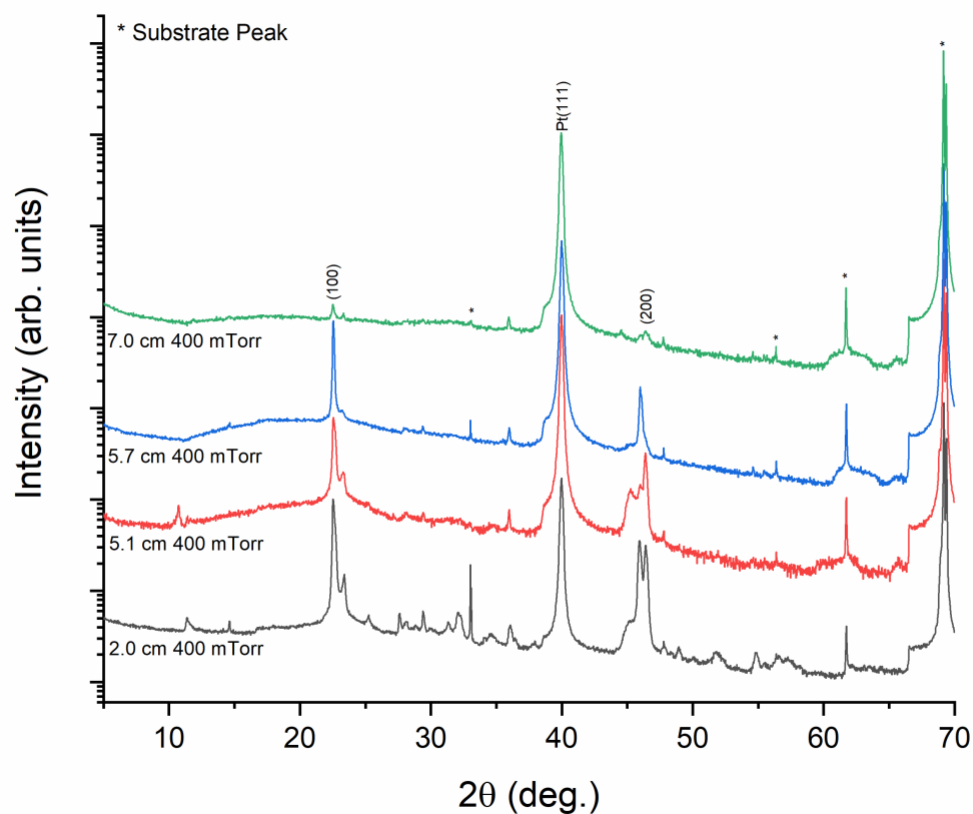
Figure 4.10: XRD patterns for depositions conducted at critical target-to-substrate distances

Figure 4.11 shows the XRD patterns for the depositions conducted at a deposition ambient pressure of 400 mTorr for varying target-to-substrate distances. In reference to the brilliant plasma plume analysis at a deposition ambient pressure of 400 mTorr shown in **Figure 4.9**, the target-to-substrate distance of 5.1 cm corresponded to the suspected optimal location just within the tip of the brilliant plasma plume, and the target-to-substrate distance of 5.7 cm was meant to correspond to the location just outside of the tip of the brilliant plasma plume. However, when the substrate was placed in the chamber and aligned to the target-to-substrate distance of 5.7 cm, the brilliant plasma plume *extended,* as shown in **Figure 4.12**, resulting in the substrate remaining located within the tip of the plasma plume, contrary to the expected location.
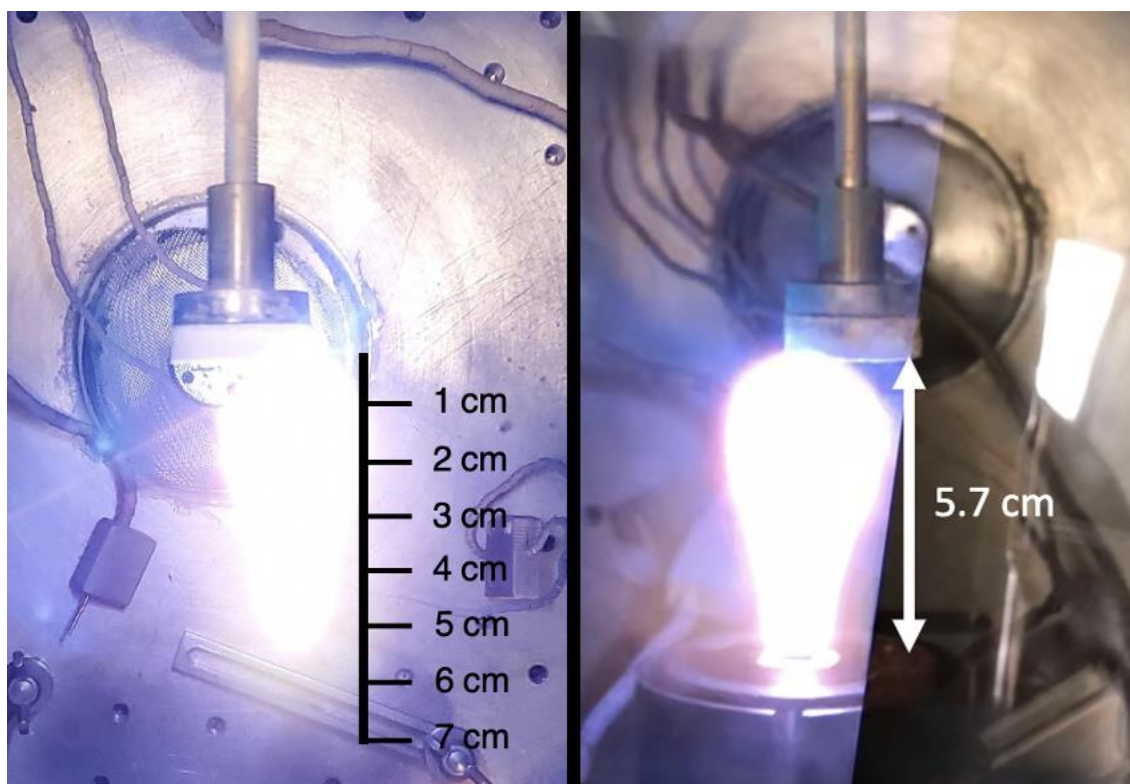
Figure 4.11: Brilliant plasma plume extension observed at a deposition ambient of 400 mTorr

The XRD pattern of this deposition indicates that these parameters produced the purest thin film containing the strongest perovskite peak, without post-deposition thermal annealing, achieved in this study. A hypothesis on the phenomena that contributes to the brilliant plasma plume extension is presented in **Section 6.2**.

4.2.2.1.3 Effect of Pulse Rate and Deposition Duration

The most dominant effect of the pulse rate of the excimer laser is on the growth rate of the thin film. At constant energy density and pulse duration, the pulse rate of the excimer laser is directly proportional to the flux of the emitted species from the bulk KNN target. The relation of the pulse rate to the flux of the emitted species is presumably linear until high pulse rates begin to result in spalling, the emission of macroparticulates generated from the preferential ablation of the target surface, increasing the resultant flux

[4]. Macroparticulate generation is an undesired feature in almost all circumstances, as such, the pulse rate is generally operated over a frequency range where spalling would not dominate the emission of material. The relation between the flux of emitted species and the growth rate of the thin film, however, is not necessarily linear, as the growth rate of the material is dependent on the dominating film formation phenomena, i.e., if the film is primarily undergoing nucleation, coalescence, or film thickness growth. In the case of nucleation and coalescence, the film formation is occurring largely parallel to the substrate surface, as such the growth rate (defined perpendicular to substrate surface) would not be linearly related to the pulse rate. In the case of film thickness growth, the film formation is occurring largely perpendicular to the substrate surface, as such the growth rate would be expected to generally be linearly related to the pulse rate. There are four processes that produce deviations from this expectation [30]. Shadowing, an effect that hinders uniform surface bombardment as a result of high surface roughness producing geometric interaction, can increase the film growth rate [30]. Low surface diffusion of adatoms can generate surface roughness, therefore facilitating shadowing [30]. High bulk diffusion can reduce the growth rate as bombarding molecules can be transported to existing voids in the material [30]. Recrystallization can either increase or decrease the film growth rate, dependent on the phase transition that takes place [30].

Figure 4.13 and Figure 4.14 show SEM cross-sections of two films of which the only differing deposition parameter was the pulse rate of the excimer laser increasing from 5 to 20 Hz.
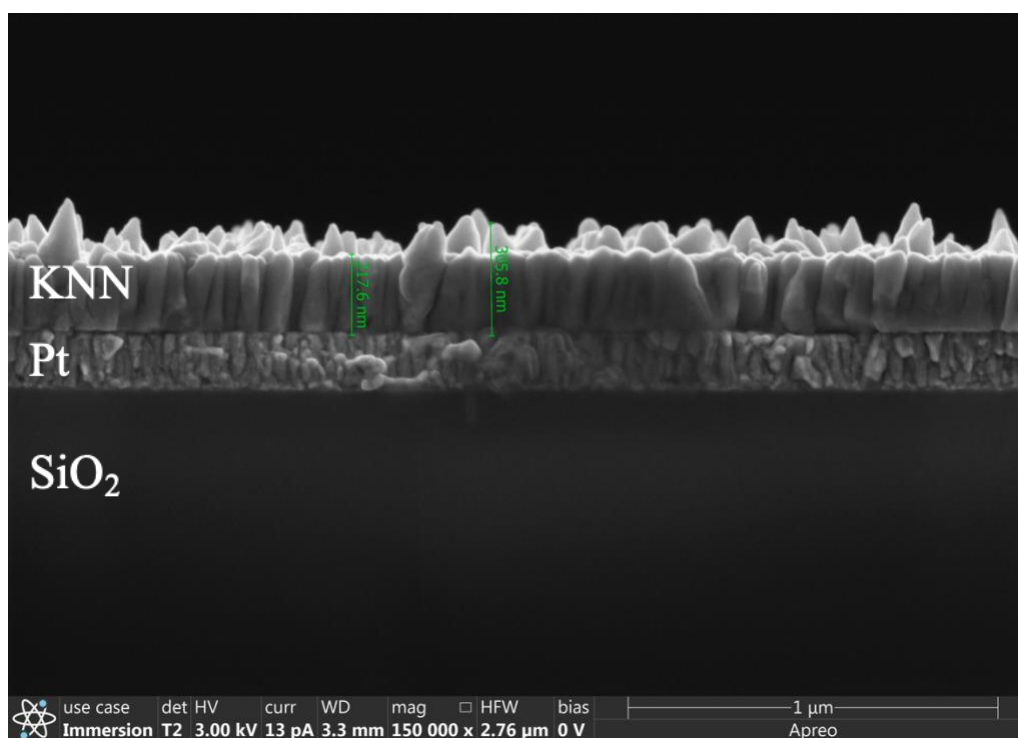
Figure 4.12: SEM cross-section of KNN thin film deposited at 5 Hz
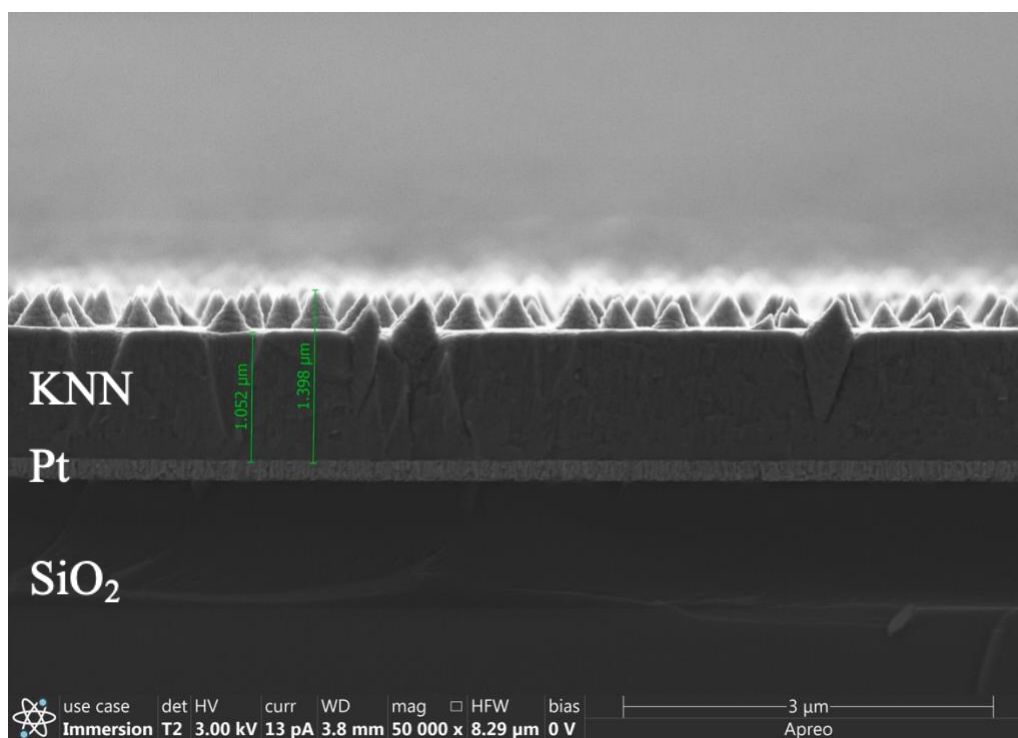
Figure 4.13: SEM cross-section of KNN thin film deposited at 20Hz

The film growth rate of these films were 1.02 and 4.66 nm/s respectively. The ratio (20 Hz: 5 Hz) of the film growth rates is 4.56, compared to the ratio of the pulse rates of 4. This indicates that the growth conditions of these films did not produce a linear relation between the pulse rate and the film growth rate. This is likely due to the high surface roughness producing the shadowing effect, thus increasing the growth rate for the rough tips of the thin film surface as a function of time.

The pulse rate would also exhibit an effect on the volatility of the alkali species during film formation. If the film deposition is conducted at high substrate temperatures, a high pulse rate would increase the rate of arriving species, allowing less time for adatoms to desorb from the film surface [4]. This affect would be best observed through XRD analysis of films containing excess alkali phases. In this study, the pulse rate was not varied at high enough substrate temperatures to directly observe this effect.

The most dominant effect of the deposition duration is on the thickness of the thin film. At constant energy density, pulse duration, and pulse rate, the deposition duration is directly proportional to the number of pulses. The deposition duration is not necessarily linearly related to the film thickness due to the same film formation phenomena detailed earlier in this section, considered with a time component. **Figure 4.14** depicts a deposition at identical parameters to the film depicted in **Figure 4.12,** but for twice the deposition duration.
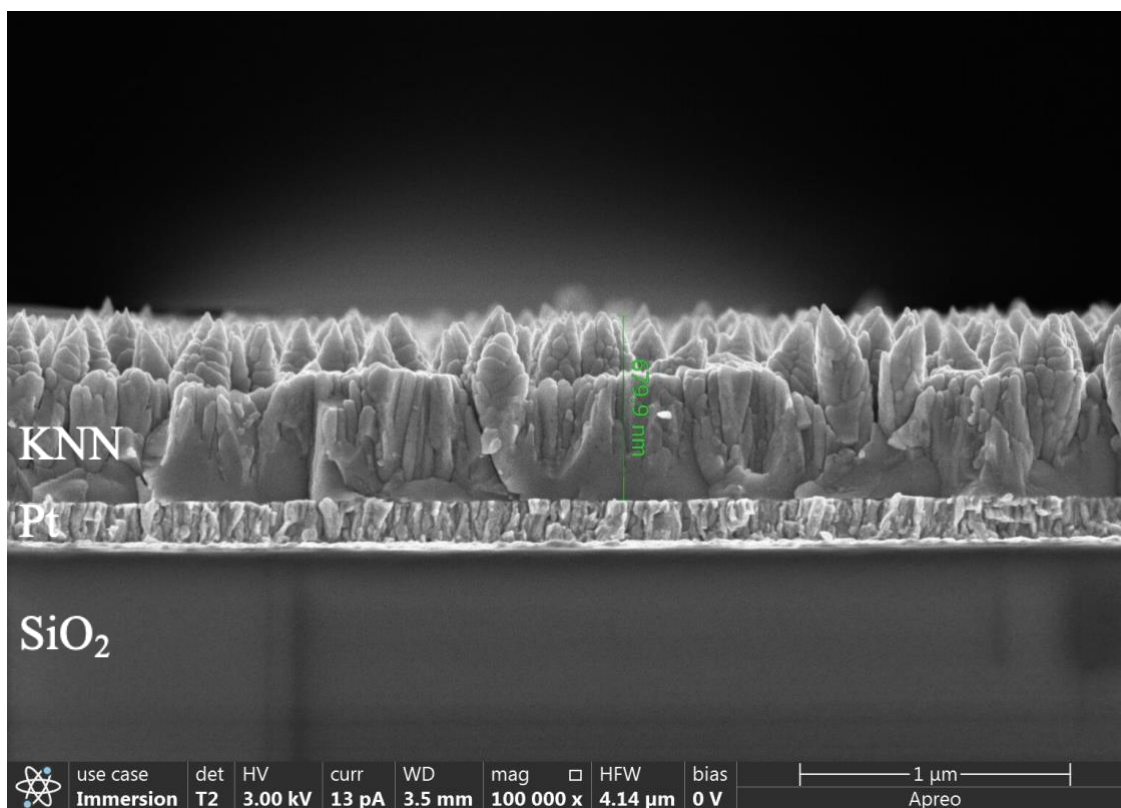
Figure 4.14: KNN thin film deposited at identical conditions to Figure 25, except twice the duration

The growth rate of this film was 1.13 nm/s compared to the 1.02 nm/s of the previous identical film for half the duration. The growth rates agree with 10% indicating that the growth conditions of these films did produce a substantial deviation from the linear relation between the pulse rate and the film growth rate.

Variation of the pulse rate and deposition duration can affect the formation of the thin film even if the number of pulses is kept constant (assuming the pulse rate to the flux of emitted species relation is in the linear range) as a high pulse rate, as previously stated, can reduce adatom desorption, but could also promote the generation of crystalline defects. As the alkali constituents of KNN volatilize readily, KNN is of particular concern for film thickness variation at a constant number of pulses. In this study the number of pulses was not varied across constant deposition conditions during process optimization, therefore this effect was not directly observed.

4.2.3 Results of Pulsed Laser Deposition Variation

The phase and microstructure of the KNN thin films was initially improved through variation in the pulsed

laser deposition parameters before a thermal anneal step was introduced into the procedure. **Figures 4.15**

shows the XRD pattern, and **Figures 4.16 and 4.17** show SEM cross-sectional and top-down images for

most phase pure KNN film achieved without a thermal annealing step, referenced at the end of **Section**

4.2.2.1.2.
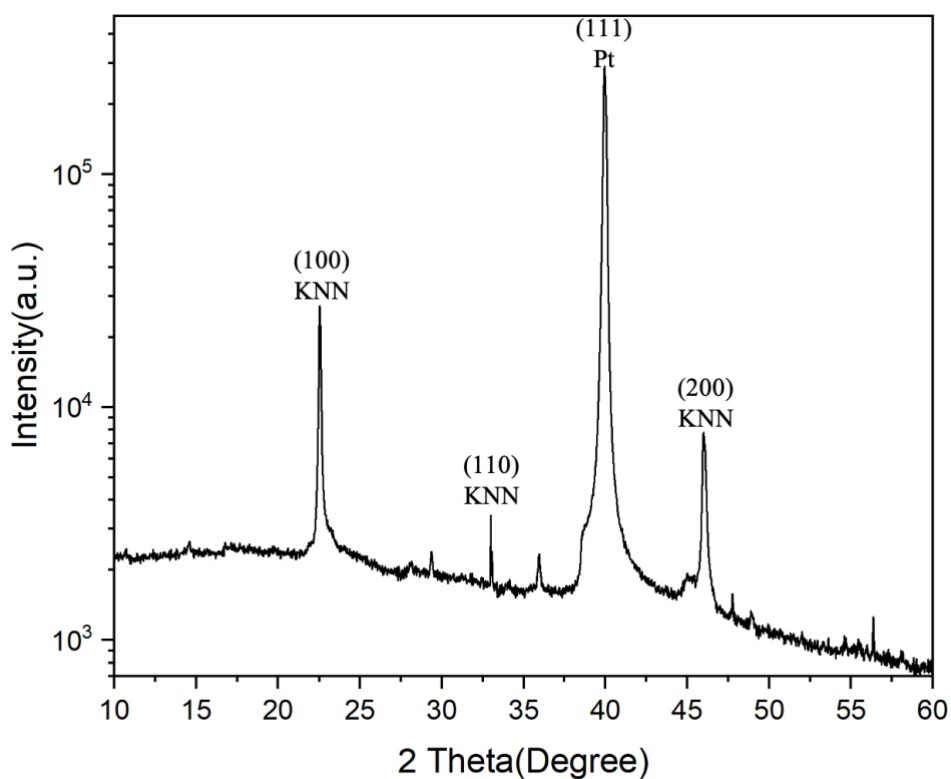
Figure 4.15: XRD pattern for the most phase pure KNN thin film produced in this study
without post-deposition annealing
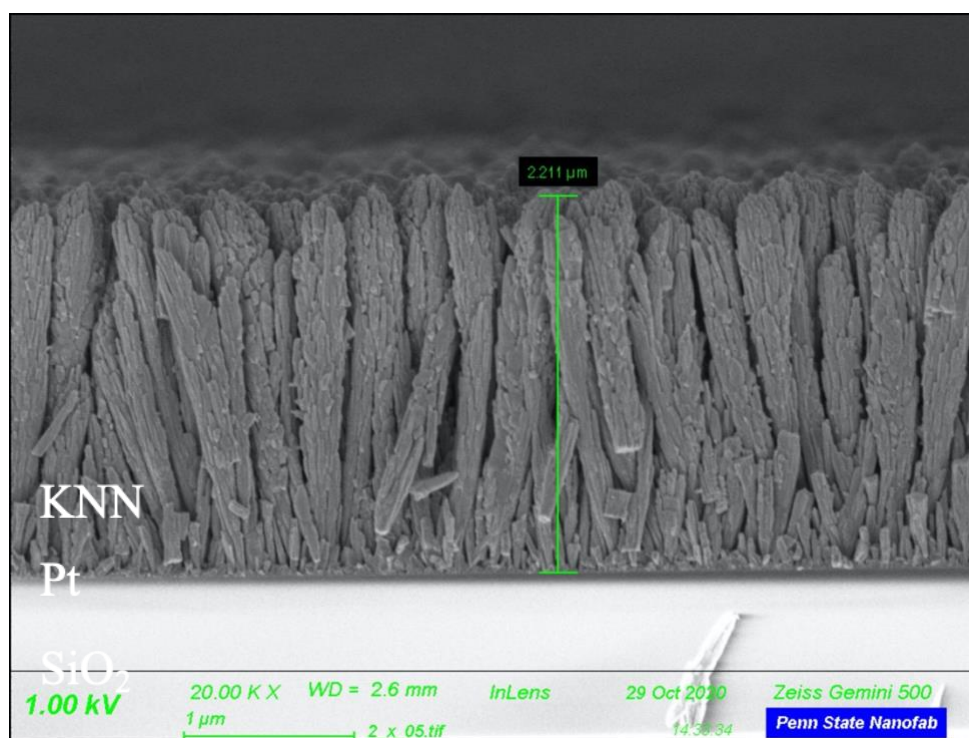
Figure 4.16: SEM cross-sectional view for most phase pure KNN thin film deposited without post-deposition annealing
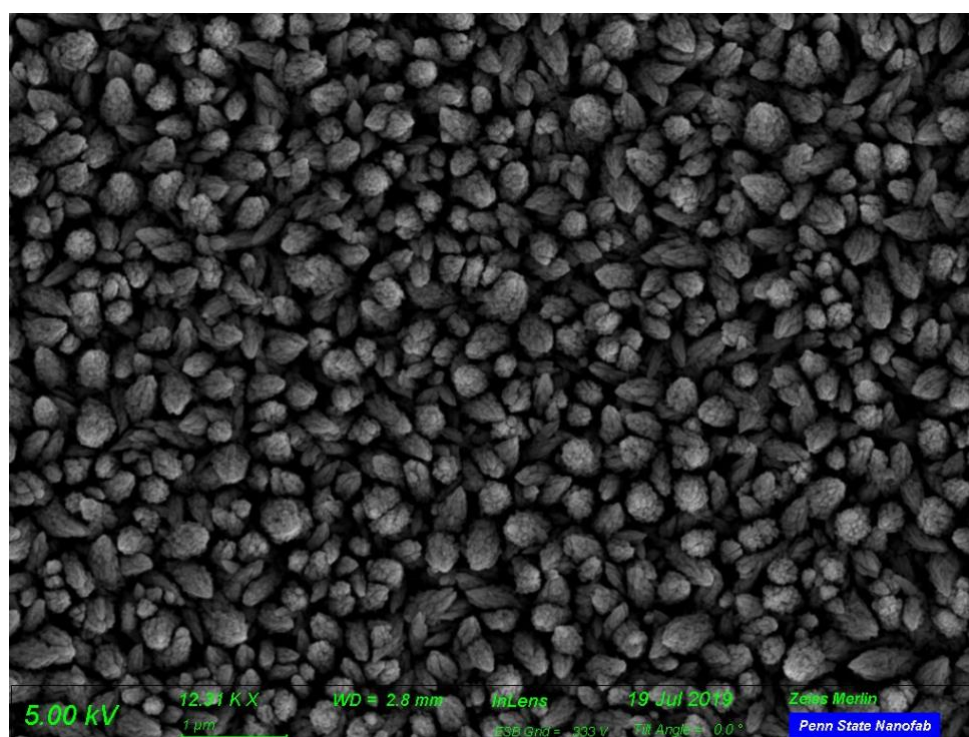
Figure 4.17: SEM top-down view for most phase pure KNN thin film deposited without post-deposition annealing

The XRD pattern indicates a strong KNN perovskite peak with minimal secondary phases. However, the SEM images of the thin film show a highly porous microstructure featuring significant void presence and high surface roughness, microstructural traits that do not predict high $e_{31,f}$ [5], but rather indicate low adatom mobility during the deposition of the thin film [31], evidence of Zone I growth. To evaluate said interpretation, with all else constant, the deposition was repeated with elevated substrate temperatures to attempt to increase adatom mobility without negatively affecting the phase purity. **Figures 4.18**, **4.19**, and **4.20** show the top-down view of these deposition attempts at substrate temperatures of 675ºC, 700ºC, and 750ºC respectively.
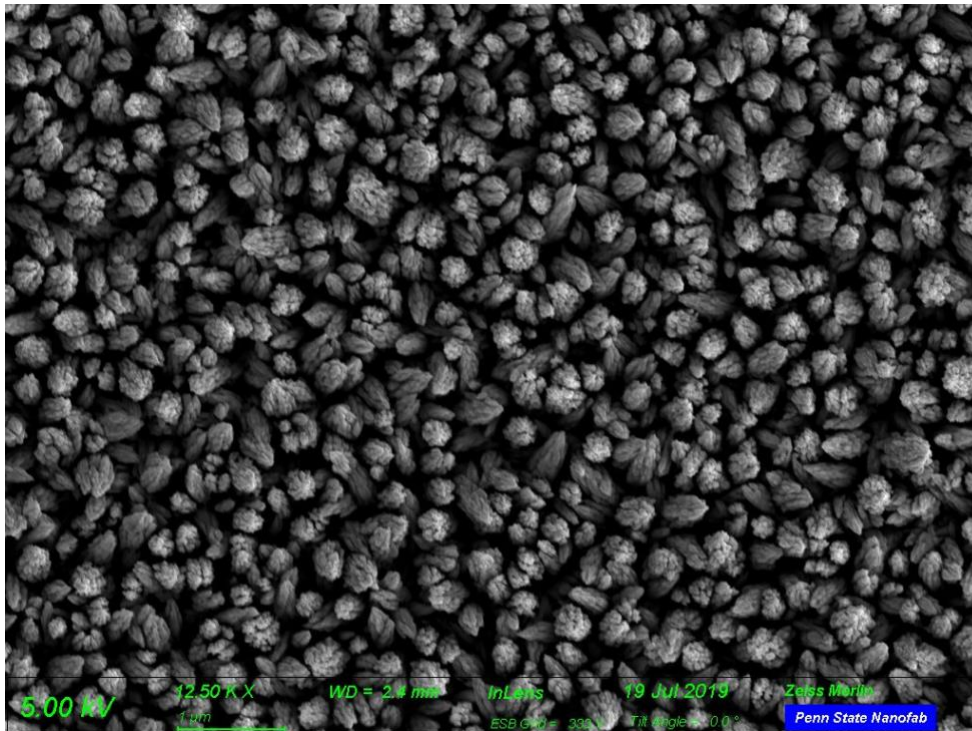
Figure 4.18: SEM top-down view of KNN at phase-pure parameters, except an increased substrate temperature of 675ºC
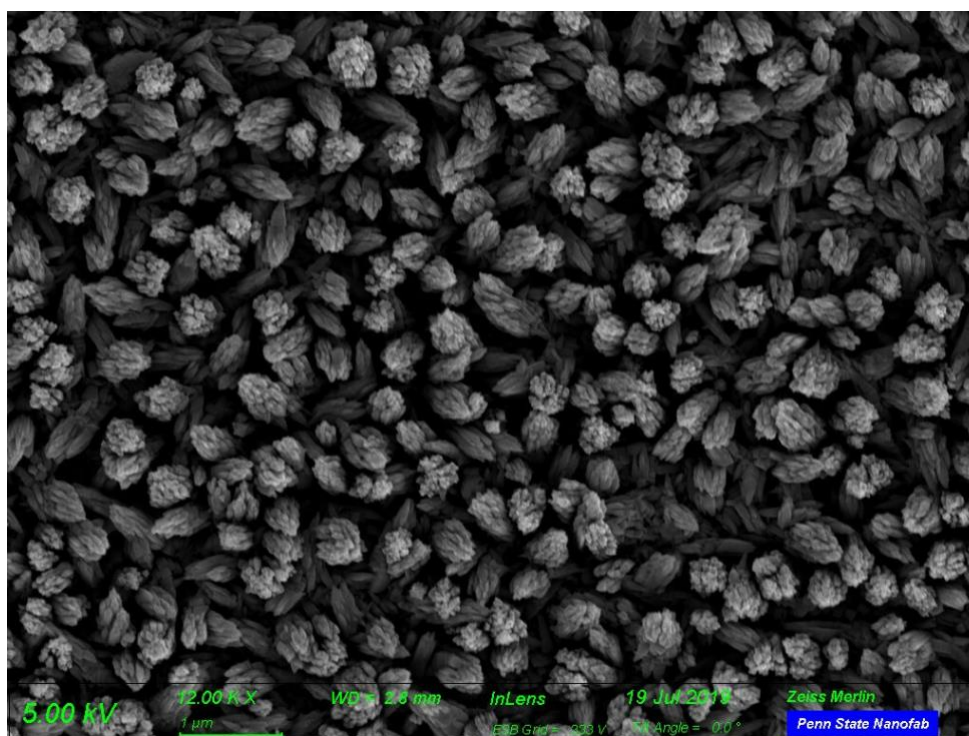
Figure 4.19 : SEM top-down view of KNN at phase-pure parameters, except an increased substrate temperature of 700ºC
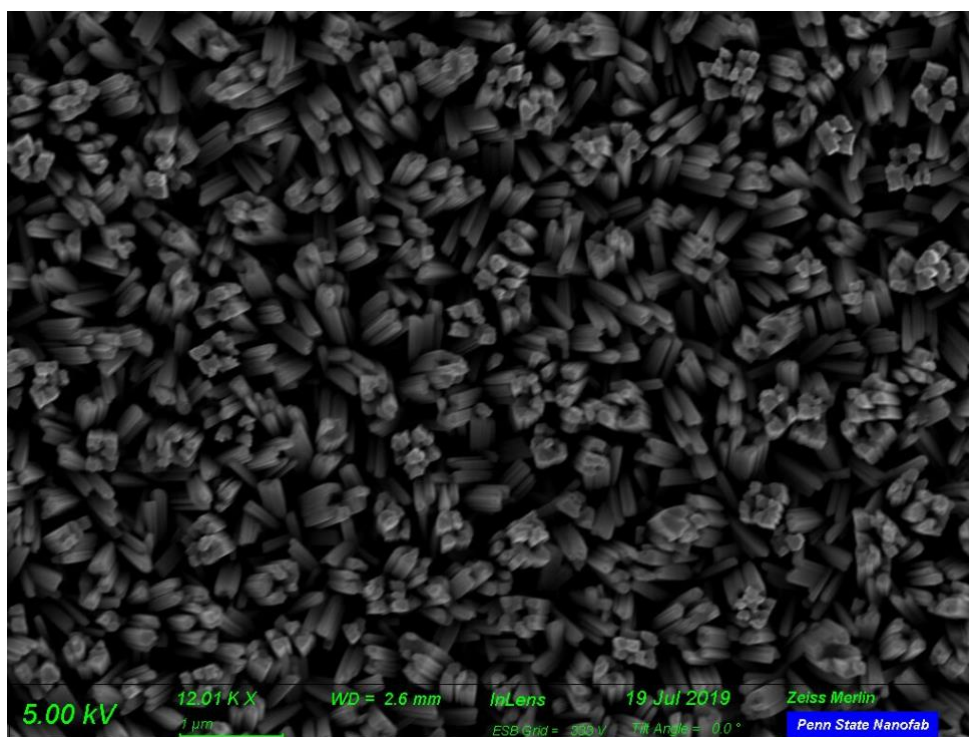
Figure 4.20 : SEM top-down view of KNN at phase-pure parameters, except an increased substrate temperature of 750ºC

Increasing the substrate temperature did not result in the desired increased densification of columnar grains, but rather produced the opposite effect, suggesting increasing adatom desorption. To evaluate said interpretation, with all else constant, the deposition was repeated at lower substrate temperatures, and a lower pulse rate based on deposition parameter effects discussed in **Section 4.2.2.1.3**, to attempt to reduce adatom desorption. The deposition duration was also increased to 10 minutes to produce films of a more desirable thickness for MEMs applications, based on the parameter-thickness relations detailed in **Section 4.2.2.1.3**. **Figures 4.21** and **4.22** show the cross-sectional imaging for these depositions conducted with a pulse rate of 5 Hz, at substrate temperatures of 600ºC and 550ºC respectively.
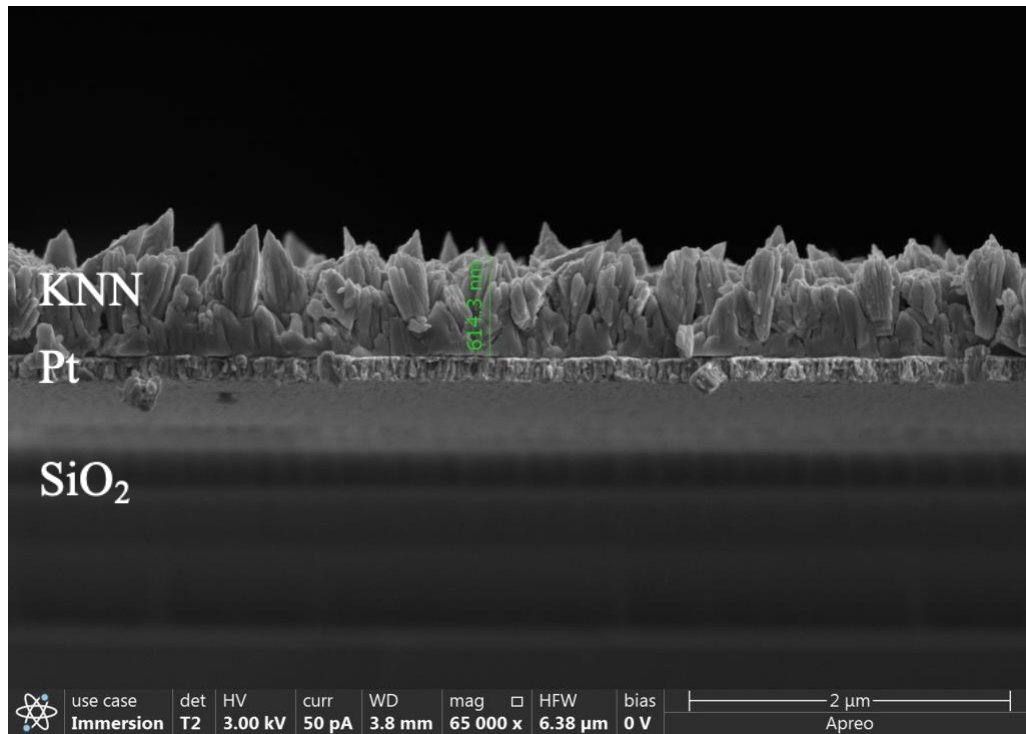
Figure 4.21: SEM cross-sectional view of KNN at phase-pure parameters, except a decreased substrate temperature of 600ºC, decreased pulse rate of 5 Hz
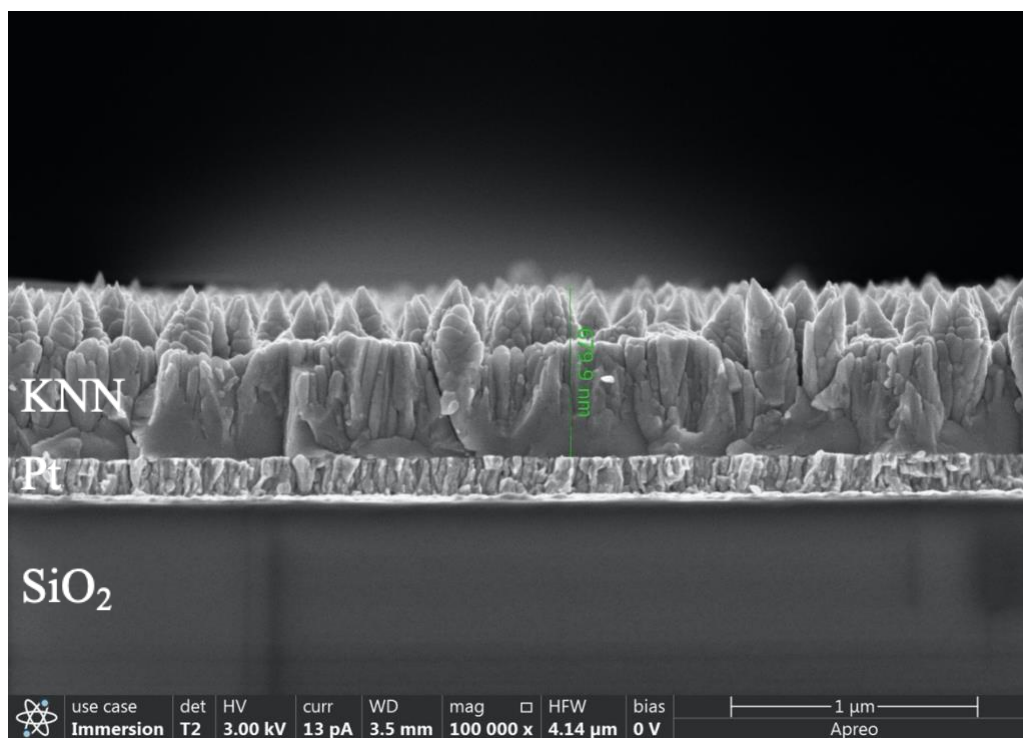
Figure 4.22: SEM cross-sectional view of KNN at phase-pure parameters, except decreased substrate temperature of 550°C, and a decreased pulse rate of 5 Hz

The SEM images show that the reduced substrate temperatures and pulse rate did increase the density of the columnar grains, but failed to significantly improve the surface roughness of the films. An important observation was made, that the structure of the film deposited at 550°C closely resembled the Stranski-Krastanov growth mode, seemingly indicating initial monolayer growth followed by three-dimensional island formation [30]. Since the microstructure of the film deposited at 550°C showed a promising microstructure, until the thickness reached approximately 500 nm, an attempt was made to confirm if the film surface and film-substrate interface energies were increasing with film growth, shifting the film growth mode from Frank-van der Merwe to Volmer Weber at approximately 500 nm, by repeating the deposition for a shorter duration. **Figure 4.23** shows the SEM cross-sectional images for an identical deposition, performed for half the duration, 5 minutes.
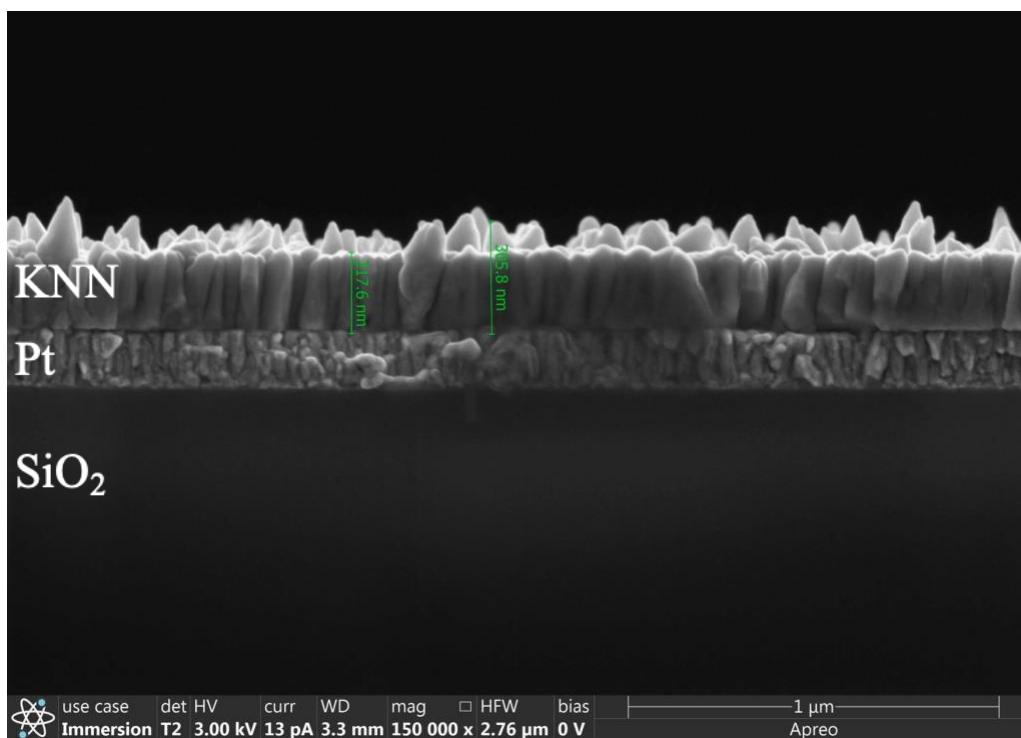
Figure 4.23: SEM cross-sectional view of KNN at parameters identical to Figure 4.20, except half the duration

The cross-sectional image of the deposition performed for 5 minutes not only still showed the presence of columns of much larger thickness, but also exhibited a ratio of the columnar growth thickness to the three-dimensional growth thickness, that is approximately identical to that of the film deposited for 10 minutes. Two conclusions were drawn from this series of depositions. The first was that the films deposited with at 550°C do not exhibit the Stranski-Krastanov growth mode, but rather follow the Volmer-Weber and Frank-van der Merwe growth modes simultaneously in different regions. The second, in conjunction with the findings discussed in **Section 4.2.2.1.2**, was that in order to produce a film with the strong perovskite phase purity exhibited at a deposition temperature of 650 °C, with the promising microstructure exhibited at a deposition temperature of 550 °C, a post-deposition thermal annealing step needed to be considered.

4.2.4 Thermal Anneal Parameters

Due to the intervention of the COVID-19 pandemic impeding the progress of this study, significantly less optimization of the thermal annealing process of KNN thin films had been conducted. As such, the majority of the recommendations for future optimization of the synthesis of high quality KNN thin films regard further optimization of the post-deposition thermal annealing process, the rationale of which is discussed in **Section 6.1**. Nevertheless, this section details the observed effects of the initial investigation into variation of the thermal annealing parameters.

4.2.4.1 Effect of Anneal Temperature and Duration

Thermal annealing was performed on several identical depositions of KNN in an attempt to improve both the microstructure and phase purity of the films. **Figure 4.24** and **4.25** depict two versions of the same KNN thin film discussed at the conclusion of **Section 4.2.3,** thermally annealed following the procedure detailed in **Section 3.1.3**, for a duration of 10 minutes, at 700ºC and 750ºC respectively.
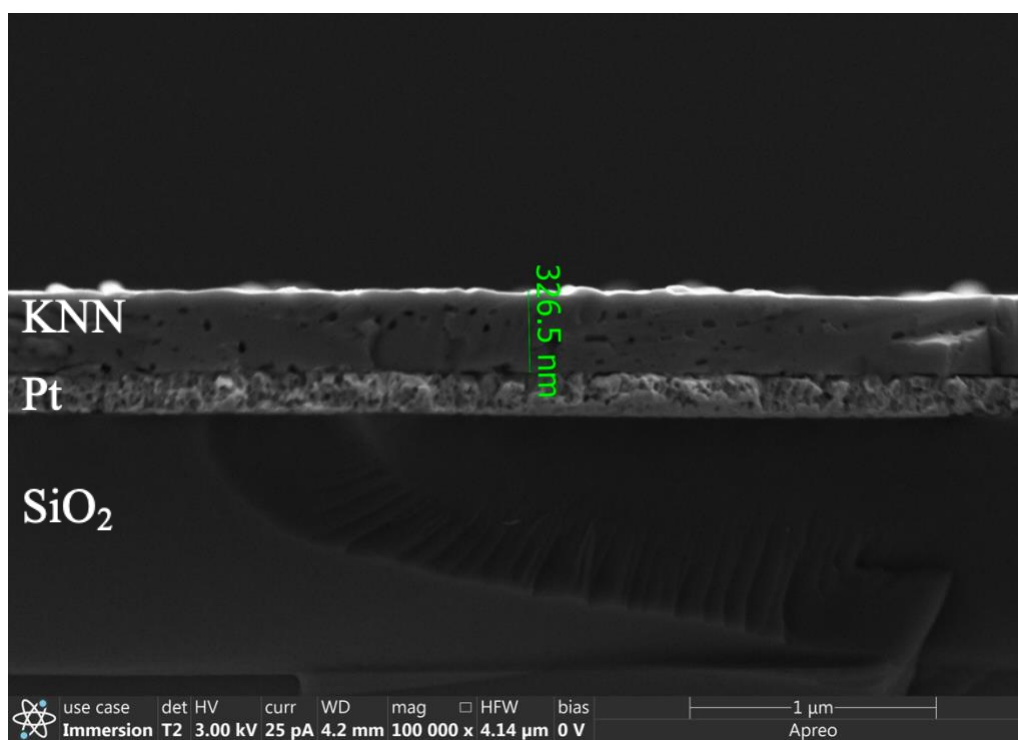
Figure 4.24: SEM cross-sectional view of KNN thin film annealed at 700ºC for 10 minutes
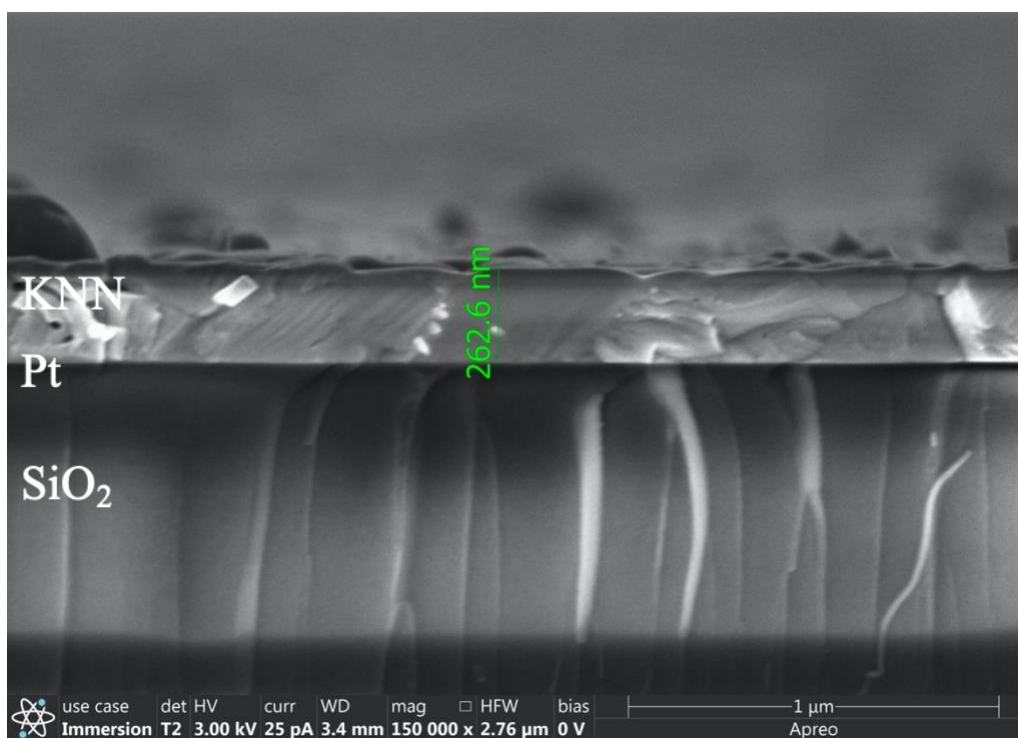
Figure 4.25: SEM cross-sectional view of KNN thin film annealed at 750ºC for 10 minutes

The surface roughness of both films improved considerably, suggesting the onset of bulk diffusion [31]. Another KNN thin-film, of identical deposition parameters, was thermally annealed at 700°C for 5 minutes. **Figure 4.26** depicts the cross-sectional image of this thin film.
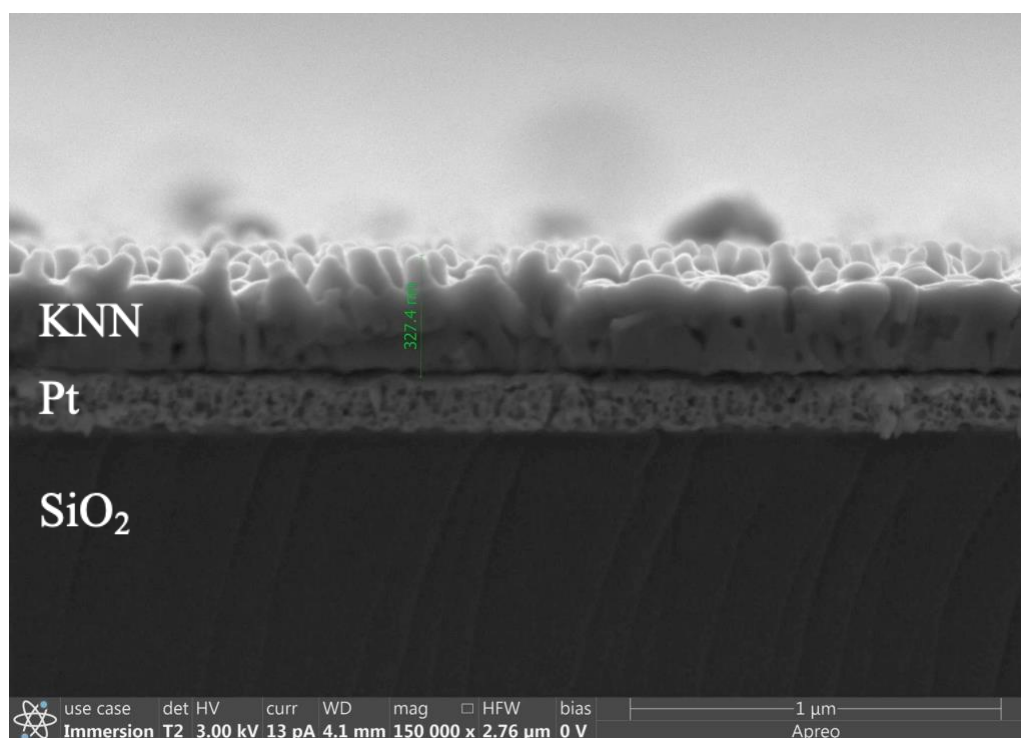
Figure 4.26: SEM cross-sectional view of KNN thin film annealed at 700°C for 5 minutes

Unsurprisingly, the microstructure of this appears was intermediate between those depicted in **Figure 4.23** and **4.24.** However, the XRD pattern of this thin film, shown in **Figure 4.27**, indicates that this film is indeed phase pure.
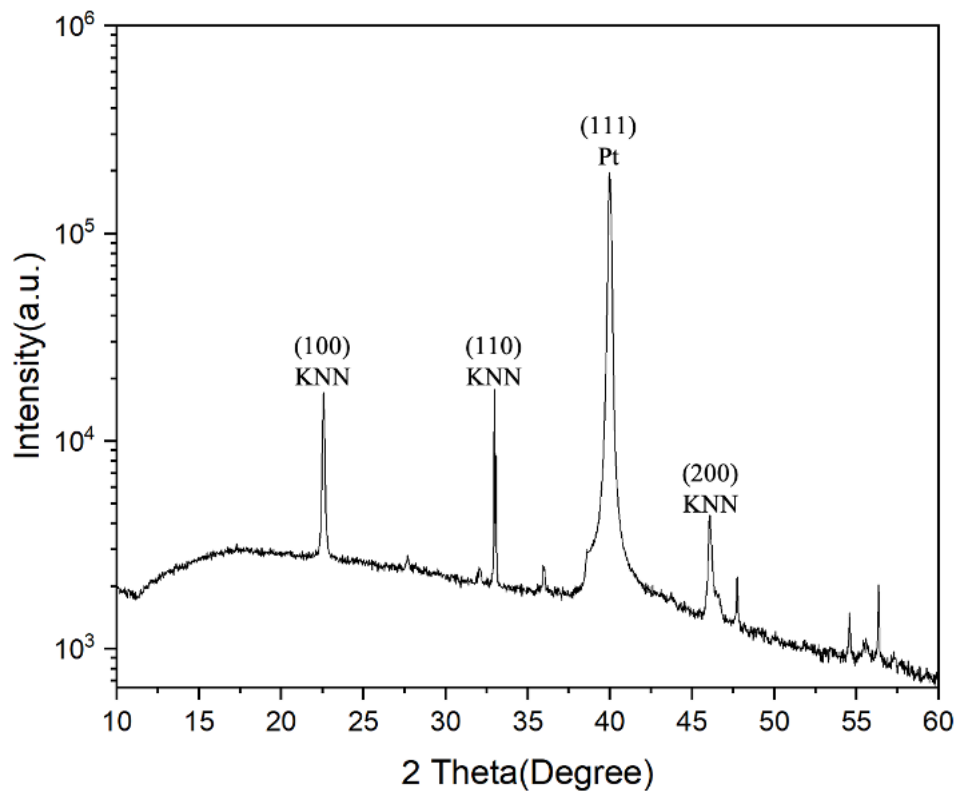
Figure 4.27: XRD pattern of KNN thin film annealed at 700ºC for 5 minutes

Though the XRD pattern shows a high phase purity, this film is not well oriented crystallographically [33].

This KNN thin film was the concluding thin film to be analyzed for this study, as such, the reported electrical measurements were obtained from said film. Due to the high surface roughness, lack of columnar microstructure, and presence of voids the electrical measurements were expected to be, and confirmed to be, suboptimal. Future work to modify the synthesis parameters to achieve optimal microstructure and phase purity is discussed in **Section 6.1**.

Chapter 5: Conclusions

This study presented the optimization reasoning and methodology for the synthesis of high-quality $(K_{0.50}Na_{0.50})NbO_3$ thin films through pulsed laser deposition, for use in piezoelectric micromachined ultrasonic transducers. The current synthesis process that produced the highest achieved quality of KNN thin films was composed of three main components: the sintering of a bulk KNN target through standard solid-state synthesis, the pulsed laser deposition of KNN thin films, and a post-deposition thermal anneal of the KNN thin films.

Experimentation of the sintering of bulk KNN targets through solid-state synthesis of the powder precursors yielded high densification at 1075 °C.

Analysis into the relation between the deposition ambient pressure and target-to-substrate distance suggested that the optimal bombardment energy for phase-pure thin films occurs at a target-to-substrate distance immediately within the tip of the brilliant plasma plume. Further analysis also observed the extension of the brilliant plasma plume upon presence of the substrate at a target-to-substrate distance beyond the expected tip of the unobstructed brilliant plasma plume. Depositions conducted at this location yielded KNN thin films of the highest phase purity, at a given deposition pressure and substrate temperature.

Analysis into the relation between the substrate temperature and the densification of the phase pure thin films yielded evidence that the low grain density was not a result of insufficient substrate temperature as decreased substrate temperatures produced higher density thin films.

The microstructure of the phase pure thin films were highly porous. Therefore, a post-deposition thermal annealing step was added to improve film microstructure without affecting phase purity. Initial investigation into thermal annealing parameters yielded promising results, showing evidence of post-deposition microstructural improvement, as well as achieving phase purity.

The highest quality KNN thin films synthesized upon the conclusion of this study exhibit non-epitaxial growth, high surface roughness, and the lack of columnar grains, features that predict poor piezoelectric performance.

The electrical characterization of the resultant film yielded a remanent polarization (P_r) of 10.7 µC/cm^2 , a maximum polarization (P) of 12.7 µC/cm^2, and a dielectric constant (ε_r) of 606. The loss tangent ($tan\delta$) was 2.8%.

The learnings demonstrated through this study strongly suggest that further optimization of the synthesis process could lead to the pulsed laser deposition of high-performance KNN thin films for use in pMUTs.

Chapter 6: Future Work

6.1 Thermal Annealing Optimization

Based on the films achieved utilizing a post-deposition thermal annealing step, detailed in **Section 4.2.4.1**, future annealing optimization should begin with lowering the annealing temperatures coupled with extended durations. These conditions will facilitate surface and bulk diffusion of the thin film atoms without producing undesired surface desorption, based on effects discussed in **Section 4.2.2.1**. The thermal annealing optimization process will be initially performed on thin films synthesized with the parameters that produced the films detailed at the beginning of **Section 4.2.3**, depicted in **Figures 4.14, 4.15,** and **4.16,** and the thin film depicted in **Figure 4.22,** as these films returned the highest quality phase purity and microstructure respectively, achieved in this study.

6.2 Brilliant Plasma Plume Extension

Though somewhat tangential to the improvement of the KNN thin films, further experimentation can be conducted to confirm the reasoning behind the extension of the brilliant plasma plume initially discussed in **Section 4.2.2.1.2,** and its subsequent production of high phase purity. It is notable that the phenomena it was only observed when the deposition ambient pressure was high, 400 mTorr. Initially discussed in **Section 2.3.2**, the ejected plasma plume is composed of two regions, the non-apparent region, and the observable brilliant region. The non-apparent region still interacts with the substrate, but as discussed in **Section 4.2.2.1.2,** is non-conducive to thin film formation due to the low energy of the emitted species [4][17].

It is the species in the brilliant region that contain sufficient energy to impact nucleation, however, the energy distribution of these species is significant [4][17], discussed in **Section 2.3.2**.

It is possible, that the increased deposition ambient pressure allowed for the high temperature stainless steel hot-stage to substantially increase the *deposition ambient temperature* of the ambient species in close proximity to the substrate. Increased energies of the ambient species would decrease the energy lost during collision with the emitted species, and therefore maintain the brilliant nature of the plume over an extended distance. It was also visually observed that the extended region was more muted and uniform in color, further supporting this hypothesis. The reduction in energy lost during collision would also serve to equilibrate the energy distribution of the emitted species in the brilliant plasma plume, which could explain the observed increase in phase purity in this region.

To test this hypothesis, an experiment to observe the degree of the extension of the plasma plume can be conducted. The extension of the plasma plume can be measured as a function of target-to-substrate distance and substrate temperature. If this conjecture holds, the plasma plume should experience decreased extension as the target-to-substrate distance increases, and increased extension as the substrate temperature significantly increases. The extension of the plasma plume should also be affected as a function of time as the total ambient increases in temperature, however due to the much larger volume of ambient species at room temperature compared to the volume of species in close proximity to the hot-stage, it would take extended periods of time to observe an effect, and is therefore an impractical method to test this hypothesis, but is an important variable to consider if this is indeed the phenomena producing the brilliant plasma plume extension.

Appendix A: Pulsed Laser Deposition Parameter Log

Dep. ID	Ann. ID	Materials		T-S Dist. [cm]	Laser Energy		Lens Pos.	Base Amb. Press. [Torr]	Sub. Temp. [ºC]	Dep. Amb. Press. [mTorr]	Pulse Rate [Hz]	Gas Flow Rate [cm³/min]	Dep. Duration [min]	Cool Press. [Torr]
		Sub.	Target [%K:%Na]		Set [mJ]	Actual [mJ]								
D1	-	Pt/Si	0:0	6.0	213	185	13	1.1 E^{-6}	550	100	10	25.9	10	100
D2	-	Pt/Si	0:0	6.0	213	185	13	1.8 E^{-7}	700	100	10	25.9	10	100
D3	-	Pt/Si	0:0	6.0	213	186	13	1.6 E^{-7}	650	100	10	25.9	10	100
D4	-	Pt/Si	0:0	6.0	213	185	13	2.1 E^{-7}	600	100	10	25.9	10	100
D5	-	Pt/Si	0:0	6.0	219	185	13	1.0 E^{-7}	650	100	10	25.9	10	100
D6	-	Pt/Si	10:5	6.0	219	185	13	1.4 E^{-7}	550	100	10	26.0	10	100
D7	-	Pt/Si	10:5	6.0	219	185	13	1.5 E^{-7}	700	100	10	26.0	10	100
D8	-	Pt/Si	10:5	6.0	219	185	13	9.6 E^{-7}	650	100	10	26.0	10	100
D9	-	Pt/Si	10:5	6.0	216	184	13	3.8 E^{-7}	650	100	10	26.0	10	100

D10	-	Pt/Si	10:5	6.0	219	185	13	1.3 E^{-7}	650	100	10	26.0	10	100
D11	-	Pt/Si	10:5	6.0	216	184	13	3.8 E^{-7}	650	100	10	26.0	10	100
D12	-	Pt/Si	10:5	6.0	216	182	13	3.6 E^{-7}	650	100	10	26.0	10	100
D13	-	Pt/Si	10:5	6.0	216	183	13	1.8 E^{-7}	650	100	10	26.0	10	100
D14	-	Pt/Si	0:0	6.0	213	183	13	1.0 E^{-6}	650	100	10	26.0	10	100
D15	-	Pt/Si	10:5	6.0	216	184	13	3.9 E^{-7}	650	200	10	26.0	10	100
D16	-	Pt/Si	10:5	6.0	216	184	13	3.3 E^{-7}	650	400	10	26.0	10	100
D17	-	Pt/Si	5:2.5	4.0	219	183	13	2.5 E^{-7}	650	100	10	26.0	10	100
D18	-	Pt/Si	5:2.5	7.0	219	182	13	1.0 E^{-6}	650	100	10	26.0	10	100
D19	-	Pt/Si	5:2.5	5.0	219	182	13	6.8 E^{-7}	650	100	10	26.0	10	100
D20	-	Pt/Si	5:2.5	6.0	219	182	13	7.0 E^{-7}	650	100	10	26.0	10	100
D21	-	Pt/Si	5:2.5	5.0	219	183	13	8.2 E^{-7}	650	200	10	26.0	10	100
D22	-	Pt/Si	5:2.5	5.3	219	183	13	8.2 E^{-7}	650	300	10	26.0	10	100
D23	-	Pt/Si	5:2.5	5.1	219	183	13	7.3 E^{-7}	650	400	10	26.0	10	100
D24	-	Pt/Si	5:2.5	5.7	219	183	13	7.8 E^{-7}	650	200	10	26.0	10	100
D25	-	Pt/Si	5:2.5	2.5	219	183	13	9.7 E^{-7}	650	400	10	26.0	10	100
D26	-	Pt/Si	5:2.5	2.0	219	184	13	9.0 E^{-7}	650	400	10	26.0	10	100

D27	-	Pt/Si	5:2.5	2.0	219	184	13	9.4 E^{-7}	650	400	10	26.0	10	100
D28	-	Pt/Si	5:2.5	5.7	219	184	13	7.7 E^{-7}	650	400	10	26.0	10	100
D29	-	Pt/Si	5:2.5	5.1	219	184	13	1.4 E^{-7}	700	400	10	26.0	10	100
D30	-	Pt/Si	5:2.5	5.7	219	184	13	9.3 E^{-7}	750	400	10	26.0	10	100
D31	-	Pt/Si	5:2.5	2.0	219	184	13	1.0 E^{-6}	650	100	10	26.0	10	400
D32	-	Pt/Si	5:2.5	7.0	219	184	13	2.7 E^{-7}	650	400	10	26.0	10	400
D33	-	Pt/Si	5:2.5	5.7	219	184	13	9.8 E^{-7}	650	400	20	26.0	5	400
D34	-	Pt/Si	5:2.5	5.7	219	184	13	2.8 E^{-7}	675	400	20	26.0	5	400
D35	-	Pt/Si	5:2.5	5.7	219	184	13	9.9 E^{-7}	700	400	20	26.0	5	400
D36	-	Pt/Si	7.5:3.75	5.7	226	185	13	6.5 E^{-7}	650	400	20	26.0	5	400
D37	-	LNO	7.5:3.75	5.7	226	185	13	6.5 E^{-7}	650	400	20	26.0	5	400
D38	-	LNO	5:2.5	5.7	220	184	13	1.0 E^{-6}	675	400	15	26.1	10	400
D39	-	LNO	5:2.5	5.7	220	184	13	1.0 E^{-6}	650	400	20	26.0	5	400
D40	-	LNO	5:2.5	5.7	219	184	13	3.3 E^{-7}	650	400	20	26.1	5	400
D41	-	LNO	5:2.5	5.7	219	184	13	5.0 E^{-7}	650	400	20	26.1	5	400
D42	-	LNO	5:2.5	5.7	219	184	13	1.0 E^{-6}	650	400	20	26.1	5	400
D43	-	LNO	5:2.5	6.0	219	184	13	1.0 E^{-6}	650	400	20	26.1	5	400

D44	-	LNO	5:2.5	5.7	219	184	13	9.4 E^{-7}	450	400	20	26.1	5	400
D45	-	LNO	10:5	5.7	219	184	13	5.1 E^{-7}	650	400	20	26.1	5	400
D46	-	LNO	10:5	5.7	219	181	13	9.1 E^{-7}	650:550	400	20	26.1	2:3	400
D47	-	Pt/Si	5:2.5	5.7	220	179	13	1.0 E^{-6}	650:550	400	20	26.1	0.5:4.5	400
D48	-	Pt/Si	5:2.5	5.7	230	180	13	1.0 E^{-6}	650:550	400	20	26.1	2:3	400
D49	-	Pt/Si	5:2.5	5.7	220	181	13	1.0 E^{-6}	650	500	20	26.0	5	400
D50	-	Pt/Si	5:2.5	5.7	220	185	13	1.0 E^{-6}	450	400	20	26.0	5	400
D51	-	Pt/Si	5:2.5	5.7	220	185	13	4.7 E^{-7}	650:550	400	20	26.1	0.5:4.5	400
D52	-	Pt/Si	5:2.5	5.1	210	180	13	2.0 E^{-7}	650	500	20	26.0	5	400
D53	-	Pt/Si	5:2.5	5.7	210	180	13	5.1 E^{-7}	650	400	20	26.0	5	400
D54	-	Pt/Si	10:5	5.7	210	180	13	7.3 E^{-7}	650	400	20	26.0	5	400
D55	-	Pt/Si	10:5	6.1	220	180	13	3.8 E^{-7}	650	500	20	26.0	5	500
D56	-	Pt/Si	5:2.5	5.7	220	184	13	1.3 E^{-7}	600	400	5	26.0	10	400
D57	-	Pt/Si	5:2.5	5.7	220	184	13	2.0 E^{-7}	550	400	5	26.0	10	400
D58	-	Pt/Si	5:2.5	5.7	220	185	13	1.1 E^{-7}	550	400	5	26.0	7	400
D59	A1	Pt/Si	5:2.5	5.7	220	185	13	1.2 E^{-7}	550	400	5	26.0	6	400
D60	A2	Pt/Si	5:2.5	5.7	220	184	13	1.9 E^{-7}	550	400	5	26.0	6	400

D61	A3	Pt/Si	5:2.5	5.7	220	185	13	1.0 E^{-7}	550	400	5	26.0	6	400
D62	A4	Pt/Si	5:2.5	5.7	220	183	13	2.2 E^{-7}	550	400	5	26.1	6	400
D63	A5	Pt/Si	5:2.5	5.7	220	185	13	1.0 E^{-6}	550	400	5	26.1	6	400
D64	A4	Pt/Si	5:2.5	5.7	220	184	13	4.5 E^{-7}	550	400	5	26.1	5	400
D65	A5	Pt/Si	5:2.5	5.7	220	184	13	2.2 E^{-7}	550	400	5	26.2	5	400
D66	A5	Pt/Si	5:2.5	5.7	220	184	13	3.5 E^{-7}	550	400	5	26.1	5	400
D67	A4	Pt/Si	5:2.5	5.7	220	183	13	8.7 E^{-7}	550	400	5	26.2	6	400
D68	A4	Pt/Si	5:2.5	5.7	220	183	13	2.2 E^{-7}	550	400	5	26.2	6	400

*Dep.: Deposition
*Dep. ID: Deposition Identification
*Ann. ID: Anneal Identification
*Sub: Substrate
*T-S Dist.: Target-to-substrate distance
*Pos.: Position
*Press.: Pressure
*Amb.: Ambient
*Pt/Si: Platinized Silicon
*LNO: Lanthanum Nickelate

Appendix B: Thermal Annealing Parameter Log

Anneal ID	Anneal Temperature [^{o}C]	Anneal Duration [min]	Anneal Ambient Composition
A1	700	10	N_2
A2	750	10	N_2
A3	800	10	N_2
A4	700	5	N_2
A5	750	5	N_2

REFERENCES

[1]   F. Jona and G. Shirane, *Ferroelectric crystals*. New York: Dover, 1993.

[2]   B. Jaffe, W. R. Cook, and H. L. Jaffe, *Piezoelectric ceramics*. Academic Press, 1971.

[3]   H. D. Megaw, *Ferroelectricity in crystals*. London: Methuen, 1957.

[4]   J.-P. Maria, "Epitaxial $Pb(Mg_{1/3}Nb_{2/3})O_3$-$PbTiO_3$ thin films," dissertation, 1998.

[5]   D. Damjanovic, "Ferroelectric, dielectric and piezoelectric properties of ferroelectric thin films and ceramics," *Reports on Progress in Physics*, vol. 61, no. 9, pp. 1267–1324, 1998.

[6]   S. Trolier-McKinstry, S. Zhang, A. J. Bell, and X. Tan, "High-Performance Piezoelectric Crystals, Ceramics, and Films," *Annual Review of Materials Research*, vol. 48, no. 1, pp. 191–217, 2018.

[7]   A. L. Kholkin, N. A. Pertsev, and A. V. Goltsev, "Piezoelectricity and Crystal Symmetry," *Piezoelectric and Acoustic Materials for Transducer Applications*, pp. 17–38, 2008.

[8]   S. Trolier-McKinstry, N. Bassiri Gharb, and D. Damjanovic, "Piezoelectric nonlinearity due to motion of 180° domain walls in ferroelectric materials at subcoercive fields: A dynamic poling model," *Applied Physics Letters*, vol. 88, no. 20, p. 202901, 2006.

[9]   S. Thomson, *Observing Phase Transitions in a Halide Perovskite Using Temperature Dependent Photoluminescence Spectroscopy*. Edinburgh Instruments, 2018.

[10]   M. D. Nguyen, M. Dekkers, E. P. Houwman, H. T. Vu, H. N. Vu, and G. Rijnders, "Lead-free $(K_{0.5}Na_{0.5})NbO_3$ thin films by pulsed laser deposition driving MEMS-based piezoelectric cantilevers," *Materials Letters*, vol. 164, pp. 413–416, 2016.

[11]   H. Soonmin, S. A. Vanalakar, A. Galal, and V. N. Singh, "A review of nanostructured thin films for gas sensing and corrosion protection," *Mediterranean Journal of Chemistry*, vol. 7, no. 6, pp. 433–451, 2018.

[12]   H. M. Smith and A. F. Turner, "Vacuum Deposited Thin Films Using a Ruby Laser," *Applied Optics*, vol. 4, no. 1, p. 147, 1965.

[13]   J. Desserre and J. F. Floy, "Interaction of laser light beam pulses with complex targets: Application to production of compound thin films," *Thin Solid Films*, vol. 29, no. 29, 1975.

[14]   S. V. Zaitsev-Zotov, A. N. Martynyuk, and E. A. Protasov, "Superconductivity in $BaPb_{1-x}Bi_xO_3$ prepared by laser evaporation method," *Fizika Tverdogo Tela*, vol. 25, no. 1, pp. 184–189, 1983.

[15]   D. Dijkkamp, T. Venkatesan, X. D. Wu, S. A. Shaheen, N. Jisrawi, Y. H. Min-Lee, W. L. McLean, and M. Croft, "Preparation of Y-Ba-Cu oxide superconductor thin films using pulsed laser evaporation from high Tc bulk material," *Applied Physics Letters*, vol. 51, no. 8, pp. 619–621, 1987.

[16]   L. Wiedeman and H. Helvajian, "Laser photodecomposition of sintered $YBa_2Cu_3O_{6+x}$: Ejected species population distributions and initial kinetic energies for the laser ablation wavelengths 351, 248, and 193 nm," *Journal of Applied Physics*, vol. 70, no. 8, pp. 4513–4523, 1991.

[17]   E. K. Müller, B. J. Nicholson, and G. L. E. Turner, "The epitaxial vapor deposition of perovskite materials," *Journal of The Electrochemical Society*, vol. 110, no. 9, p. 969, 1963.

[18]   Y. Qiu, J. Gigliotti, M. Wallace, F. Griggio, C. Demore, S. Cochran, and S. Trolier-McKinstry, "Piezoelectric Micromachined Ultrasound Transducer (PMUT) arrays for integrated sensing, actuation and imaging," *Sensors*, vol. 15, no. 4, pp. 8020–8041, 2015.

[19]   I. Ladabaum, X. Jin, H. T. Soh, A. Atalar, and B. Khuri-Yakub, "Surface micromachined capacitive ultrasonic transducers," *IEEE Transactions on Ultrasonics, Ferroelectrics and Frequency Control*, vol. 45, no. 3, pp. 678–690, 1998.

[20]   P. C. Eccardt and K. Niederer, "Micromachined ultrasound transducers with improved coupling factors from a CMOS compatible process," *Ultrasonics*, vol. 38, no. 1-8, pp. 774–780, 2000.

[21] C. Y. Cheng, A. Dangi, L. Ren, S. Tiwari, R. R. Benoit, Y. Qiu, H. S. Lay, S. Agrawal, R. Pratap, S.-R. Kothapalli, T. E. Mallouk, S. Cochran, and S. Trolier-McKinstry, "Thin Film PZT-Based PMUT Arrays for Deterministic Particle Manipulation," *IEEE Transactions on Ultrasonics, Ferroelectrics, and Frequency Control*, vol. 66, no. 10, pp. 1606–1615, 2019.

[22] F. Akasheh, T. Myers, J. D. Fraser, S. Bose, and A. Bandyopadhyay, "Development of piezoelectric micromachined ultrasonic transducers," *Sensors and Actuators A*, vol. 111, pp. 275–287, 2004.

[23] A. Popovič, L. Bencze, J. Koruza, and B. Malič, "Vapour pressure and mixing thermodynamic properties of the $KNbO_3$–$NaNbO_3$ system," *RSC Advances*, vol. 5, no. 93, pp. 76249–76256, 2015.

[24] B. Malic, D. Jenko, J. Bernard, J. Cilensek, and M. Kosec, "Synthesis and Sintering of $(K,Na)NbO_3$ Based Ceramics," *MRS Proceedings*, vol. 755, 2002.

[25] L. Egerton and C. A. Bieling, "Isostatically hot-pressed sodium-potassium niobate transducer material for ultrasonic devices," *American Ceramic Society Bulletin*, vol. 47, no. 12, pp. 1151–1156, 1968.

[26] K. Shibata, F. Oka, A. Nomoto, T. Mishima, and I. Kanno, "Crystalline structure of highly piezoelectric $(K,Na)NbO_3$ films deposited by RF magnetron sputtering," *Japanese Journal of Applied Physics*, vol. 47, no. 12, pp. 8909–8913, 2008.

[27] M. N. R. Ashfold, F. Claeyssens, G. M. Fuge, and S. J. Henley, "Pulsed laser ablation and deposition of thin films," *Chemical Society Reviews*, vol. 33, pp. 23–31, 2004.

[28] J. A. Thornton, "Structure-Zone Models of Thin Films," *Modeling of Optical Thin Films*, 1988.

[29] M. D. Nguyen, E. P. Houwman, M. Dekkers, and G. Rijnders, "Strongly enhanced piezoelectric response in lead zirconate titanate films with vertically aligned columnar grains," *ACS Applied Materials & Interfaces*, vol. 9, no. 11, pp. 9849–9861, 2017.

[30] N. Kaiser, "Review of the fundamentals of thin-film growth," *Applied Optics*, vol. 41, no. 16, p. 3053, 2002.

[31] R. Messier, A. P. Giri, and R. A. Roy, "Revised structure zone model for thin film physical structure," *Journal of Vacuum Science & Technology A: Vacuum, Surfaces, and Films*, vol. 2, no. 2, pp. 500–503, 1984.

[32] Y. Saito, H. Takao, T. Tani, T. Nonoyama, K. Takatori, T. Homma, T. Nagaya, and M. Nakamura, "Lead-free piezoceramics," *Nature*, vol. 432, pp. 84–87, 2004.

[33] S. Trolier-McKinstry and P. Muralt, "Thin Film Piezoelectrics for MEMS," *Journal of Electroceramics*, vol. 12, no. 1/2, pp. 7–17, 2004.

ACADEMIC VITA

KALEB JESSE STERLING

The Pennsylvania State University   **Aug. 2017 – May 2021**
- College of Earth and Mineral Science
- Materials Science and Engineering (B.S.)
  - Minor: Electronic and Photonic Materials (EPM)
- Schreyer Honors College
  - Thesis: Synthesis of KNN Thin Films Through Pulsed Laser Deposition for Piezoelectric Micromachined Ultrasonic Transducers

Work Experience

Engineering Intern – Parker Lord Corporation – Cary, NC   **June 2020 – Aug. 2020**
- Conducted laboratory research into silicone-based thermal interface materials (TIMs) for the Advanced Chemical Technology group in the Assembly and Protection Solutions division

Undergraduate Researcher – NSF MRSEC – State College, PA   **June 2019 – Aug. 2019**
- Completed the Interdisciplinary Materials and Physics Research Experience for Undergraduates
- Performed process optimization for the synthesis of piezoelectric ceramic $(K_{0.5}Na_{0.5})NbO_3$ (KNN) thin films through pulsed laser deposition

Leadership Experience

Philanthropy Chair – Tau Epsilon Phi Fraternity – State College, PA   **Dec. 2019 – May 2021**
- Directed and facilitated community outreach and THON fundraising for the Epsilon Phi chapter

Relevant Projects

The Pennsylvania State University – Materials Research Institute   **Aug. 2019 – May 2021**
- Pursuing research into synthesizing high quality KNN thin films to produce environmentally-friendly piezoelectric micromachined ultrasonic transducers (pMUTs)

Technical Skills

Equipment Operation – Parker Lord Corporation
- Discovery HR 2 Rheometer, Instron Dual Column Tabletop Testing System, Thermal Interface Material tester (TIM), Hot Disk Thermal Analyzer

Equipment Operation – The Pennsylvania State University Nanofabrication Laboratory
- Scanning electron microscopy (SEM), x-ray powder diffraction (XRD), cold isostatic press (CIP), rapid thermal processing furnace (RTP), KrF excimer laser, vacuum chamber operation [10^{-7} torr]

Computer Software
- Crystal Maker, JADE, Solidworks 3D CAD, Autodesk Fusion 360 CAD

Programming Languages
- Python, MATLAB, C, Java

Relevant Coursework
- Properties and Characteristics of Electronic and Photonic Materials, Synthesis and Processing of Electronic and Photonic Materials, Materials Process Kinetics, Computational Materials Science and Engineering, Materials Characterization
- Thermal Properties of Materials, Thermodynamics of Materials, Electric and Magnetic Properties of Materials, Mechanical Properties of Materials
- Polymer Materials, Crystal Chemistry, Organic Chemistry